Tiltwing Transition Flight Analysis Using High-Fidelity CFD

David Garcia Perez* **Patricia Ventura Diaz** **Anthony Sanguinetti**
Science and Technology Corporation
NASA Ames Research Center
Moffett Field, California, USA

Seokkwan Yoon
NASA Advanced Supercomputing Division
NASA Ames Research Center
Moffett Field, California, USA

ABSTRACT

Transition from hover to forward flight and vice versa represents the most critical flight phase of tiltwing aircraft. Despite its importance to ensure a safe operation, the aerodynamics of this maneuver are not sufficiently understood. This paper focuses on the study of transition flight for NASA's six-passenger tiltwing air taxi by means of high-fidelity computational fluid dynamics simulations. On the basis of a static trim solution, four points within the transition corridor are analyzed: transition mode at wing tilt angles of 60° and 44°, and airplane mode at airspeeds of 110 kt and 155 kt. We investigate the balance of forces and moments for rotor-borne and wing-borne regimes, and how rotor-on-rotor and rotor-on-wing interactions affect performance. The simulations indicate that during the early stages of transition, the vortices remain in close proximity to the proprotors, inducing large fluctuations on the order of the mean blade loading. Additionally, the blowing and swirling effects of the proprotor wakes delay flow separation over a portion of the wing. The mid-transition conditions appear to be critical, with extensive regions of separated flow over the wing. In airplane mode, proprotor-wing slipstream effects can be exploited to enhance lift generation. The results of this paper contribute to a deeper understanding of the complex aerodynamic interactions during transition flight to enable a safer and more efficient operation of tiltwing aircraft.

NOTATION

Greek symbols

Symbol	Description
α	Angle of attack
δ_e	Elevator deflection
δ_f	Flap deflection
μ	Advance ratio
Ω	Rotor rotational speed
ψ	Azimuth angle
ρ	Air density
Θ	Airframe pitch angle
θ_0	Rotor collective pitch angle

Roman symbols

Symbol	Description
a	Air speed of sound
b	Wing span
b_h	Horizontal tail span
c	Local blade chord
D	Aerodynamic drag force
f	Generalized force or moment
F_x	Horizontal force in body axes
F_z	Vertical force in body axes
i_w	Wing tilt angle
L	Aerodynamic lift force
M	Mach number
$M^2 c_c$	Blade section chord force coefficient
$M^2 c_m$	Blade section pitch moment coefficient
$M^2 c_n$	Blade section normal force coefficient
M_y	Pitch moment in body axes
q	Air dynamic pressure
R	Rotor radius
r	Radial coordinate
V	Velocity with respect to the air
v_i	Rotor induced velocity
W	Aircraft weight
y^+	Non-dimensional viscous wall spacing

Subscripts

Subscript	Description
CII	CAMRAD II
OF	OVERFLOW
e	Elevator
f	Flap
p	Proprotor
w	Wing

*Corresponding author: david.garciaperez@nasa.gov
Presented at the Vertical Flight Society's 80th Annual Forum & Technology Display, Montréal, Québec, Canada, May 7–9, 2024.

INTRODUCTION

Urban air mobility (UAM) is the vision of a new transportation paradigm that will enable safe and efficient mobility of people and goods through the airspace in urban and suburban areas. Although this idea has existed for decades with helicopters, its implementation has been limited due to high costs and noise. Only recently has it been revitalized with advancements in aircraft technologies, such as electric propulsion, lightweight materials, and autonomous flight, that may potentially shift aerial inter-city travel from traditional helicopter flights to newer vehicle concepts that offer more efficient, sustainable, and technologically advanced solutions.

Over the last few years, much research at NASA has focused on the development of UAM vehicles or air taxis. In particular, NASA's Revolutionary Vertical Lift Technology (RVLT) project has been developing tools and datasets to support the design of advanced vertical-lift aircraft (Ref. 1). RVLT has established a catalog of conceptual air vehicles with the objective of guiding research activities in a direction that supports aircraft development in emerging aviation markets (Ref. 2). RVLT has also been expanding various software packages to integrate individual discipline-based prediction tools into a unified toolchain. This toolchain has been applied to several concept vehicles for the practical design of quieter UAM aircraft: quadrotor, side-by-side, lift-plus-cruise, quiet single-main rotor, and tiltwing aircraft configurations (Ref. 3).

This work focuses on the analysis of the tiltwing configuration (Ref. 4). Tiltwings are a versatile class of aircraft that combine the vertical take-off and landing (VTOL) capabilities of conventional helicopters and the long-range, high-speed forward flight of fixed-wing aircraft. NASA's tiltwing design for UAM features a tilting main wing with six five-bladed proprotors located ahead of the leading edge, and a T-tail configuration with two five-bladed tilting proprotors located at the tips. The vehicle has two flight states shown in figure 1: helicopter mode and airplane mode. In helicopter mode, the proprotors spin in an approximately horizontal plane, providing sufficient thrust to support the aircraft's weight. The desired attitude and motion are achieved via rotor collective control. In airplane mode, the proprotors spin in a quasi-vertical plane, generating the propulsive force to allow the vehicle to move forward, whereas the wing provides the required lift. In this case, control actuators include flaps and elevator for longitudinal motion, and ailerons and rudder for lateral-directional motion. The conversion between each state is accomplished by traversing a transition corridor defined by different combinations of airspeed and wing tilt angle. Transition flight is a complex aeromechanical operation that entails flight stability and control issues, since the thrust and lift requirements change dynamically as the wing and proprotors tilt to accelerate or decelerate the vehicle. During this maneuver, separated flow over the wing is a concern for safety, performance, and controllability. Johnson et al. (Ref. 5), in a preliminary analysis of this configuration, suggested that the wing is operating near or just beyond stall during conversion. Higher-fidelity aerodynamic analyses are required to further investigate this behavior.

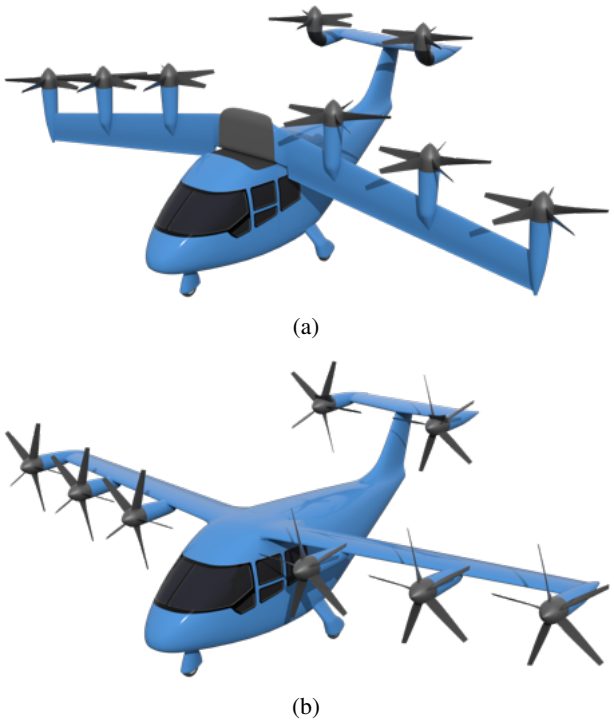

(a)

(b)

Figure 1: Rendering of NASA's tiltwing air taxi for UAM: (a) helicopter mode and (b) airplane mode.

Due to its versatility, the tiltwing configuration has recently received special attention. Several authors (Refs. 6–8) have studied transition flight focusing on trajectory optimization, but the use of low-order aerodynamic models did not properly account for strong aerodynamic interactions, flow separation, or unsteady aerodynamic phenomena. Droandi et al. (Ref. 9) compared the aerodynamic solutions of low- and medium-fidelity methods and found significant discrepancies in wing loads during mid-transition. High-fidelity simulations have the potential to provide a more accurate description of the aerodynamics. Previous high-fidelity computational fluid dynamics (CFD) work by Ventura Diaz et al. includes simulations of NASA's quiet single-main rotor helicopter (Refs. 10, 11), NASA's quadrotor isolated rotors (Ref. 12) and quadrotor complete vehicle (Ref. 13), and NASA's side-by-side air taxi concept (Refs. 14, 15). However, none of these vehicles undergoes transition maneuvers where the lift function is exchanged between various components —proprotors to wing and vice versa. More recently, Garcia Perez et al. (Refs. 16,17) conducted high- and medium-fidelity simulations of NASA's tiltwing concept in hover and cruise. The study merely aimed to analyze the aerodynamics in these flight conditions since the initial geometry did not include wing/tail control surfaces and could not be properly trimmed.

Despite the recent research on this configuration, there is a lack of studies on transition flight by means of high-fidelity tools. To fill this niche, this paper presents high-fidelity simulations of NASA's tiltwing air taxi in different phases of transition flight. The flow solver is coupled with a comprehensive code to obtain an accurate vehicle trim. The main objective is to study the airloads, wake geometry, and performance with a

focus on rotor-on-rotor and rotor-on-wing interactions.

NUMERICAL APPROACH

NASA's OVERFLOW CFD flow solver (Ref. 18) is utilized in this study. OVERFLOW is a finite-difference, structured overset grid, high-order accurate Navier-Stokes flow solver. NASA's Chimera Grid Tools (CGT) (Ref. 19) software package is used for the overset grid generation of the proprotors and the complete vehicle. OVERFLOW is loosely coupled with the helicopter comprehensive code CAMRAD II (Ref. 20).

Overset Grids

The use of overset grids simplifies the grid generation for complex geometries. Components are broken down into simpler shapes and individual grids are generated for each one. The near-body (NB) grids are attached to the bodies and move with them, whereas a collection of stationary Cartesian off-body (OB) grids cover the surroundings. Overset grids offer flexibility and control over grid generation and quality, since the NB grids can have different resolutions, topologies, and boundary conditions, and allow for relative motion between components. With CGT, the overset grid generation process may be decomposed into four steps: geometry processing, surface grid generation, volume grid generation, and domain connectivity (Ref. 19).

The geometry was obtained from a computer-aided design (CAD) model. Figure 2a shows the CAD geometry used for the tiltwing vehicle in transition flight. In solid modeling, the boundary representation (BRep) of an object describes its boundaries holding both the topological entities and the geometric components (Ref. 21). A pre-processing step generates discrete surface representations from the analytical BRep solid contained in STEP or IGES files. Access to the model topology and entities is accomplished through EGADS (the Engineering Geometry Aircraft Design System) API, which is a foundational component of the Engineering Sketch Pad (Ref. 21). For each body in the geometry, the `egads2srf` tool generates a surface grid file containing a set of structured surface patches on tessellated untrimmed BRep faces. Figure 2b shows the structured untrimmed patches obtained using EGADS for the tiltwing aircraft. A curve grid file is also created that contains structured curves on tessellated BRep edges. Both files are used as inputs in the overset surface grid generation step.

Once the geometry has been processed as reference curve and surface files, structured surface grids are generated using a combination of algebraic and hyperbolic methods. Figure 3 shows the resulting overset surface grids for the complete vehicle. Table 1 gathers the information used to generate the geometry. The blades use the same airfoils as the XV-15 rotor (Ref. 22), scaled down to the propeller size. The root cutout is $r = 0.2R$. Each blade has a taper of $\lambda = 0.95$. Surface grid resolution on the proprotor blades is clustered in high pressure-gradient regions: leading and trailing edge in the chordwise direction, and root and tip in the spanwise direction. The wing flaps extend from the root to 87 % of

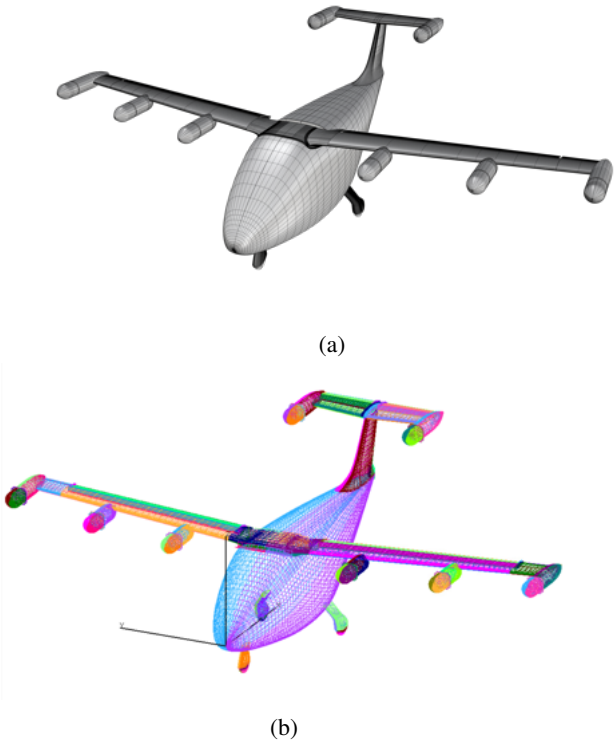

(a)

(b)

Figure 2: The tiltwing vehicle air taxi airframe: (a) CAD geometry and (b) structured untrimmed patches obtained with EGADS. The patches are used as reference surfaces to generate the overset grids.

Table 1: Tiltwing geometric parameters.

	Parameter	Value
Rotor	Number of blades per rotor	5
	Radius R	3.6496 ft
	Root chord c_{root}	0.5887 ft
	Tip chord c_{tip}	0.5593 ft
	Thrust-weighted solidity σ	0.2471
Main wing	Span b	44.4 ft
	Area A	128 ft^2
	Aspect ratio AR	15.3
Empennage	Horizontal tail span b_{h}	10.2 ft
	Horizontal tail area A_{h}	18.4 ft^2
	Vertical tail span b_{v}	5.28 ft
	Vertical tail area A_{v}	18.4 ft^2
Fuselage	Length l_{f}	28 ft

the semispan with a chord equal to 40 % of the wing chord. Similarly, the elevator extends for the full span with a chord equal to 40 % of the tail chord. Since the chordwise length of the vertical tail extends to more than 60 % of the root chord of the horizontal tail, the elevator was split in two halves to facilitate grid generation. Figure 4 shows the CAD models used for the control surfaces.

With sufficient overlap for the overset surface grids, the vol-

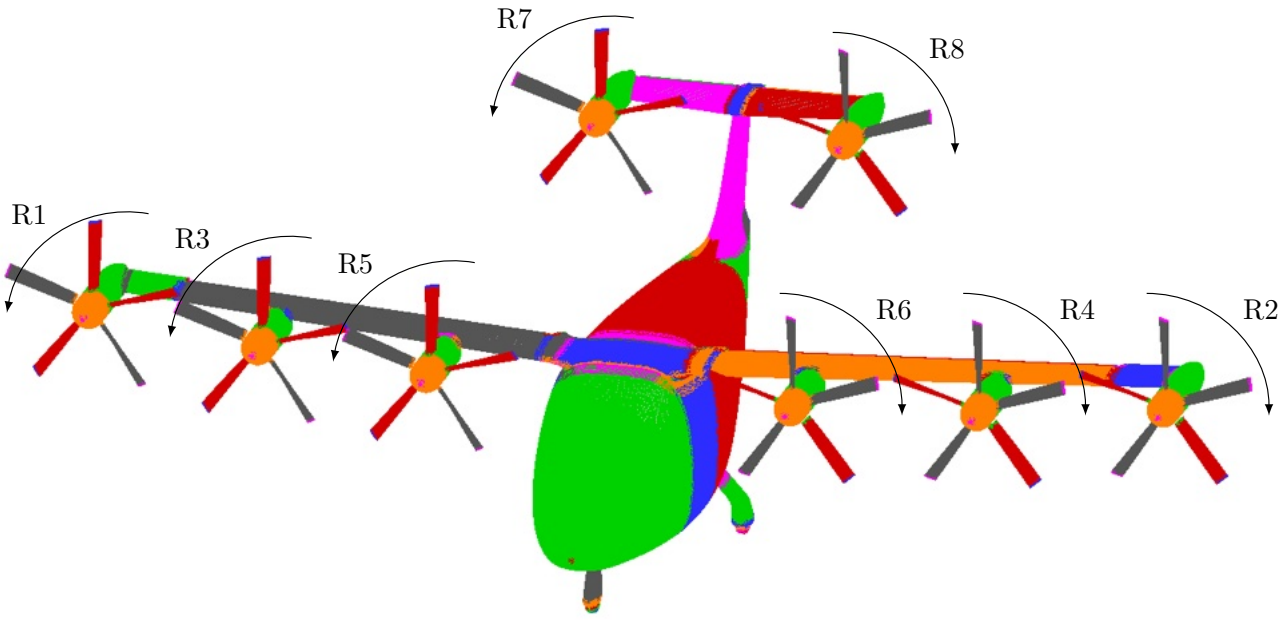

Figure 3: Tiltwing overset surface grids for the complete vehicle, which includes eight proprotors with their corresponding nacelles, fuselage, wing, flaps, tail, elevator, and landing gear. The naming convention and spin direction of the proprotors are indicated.

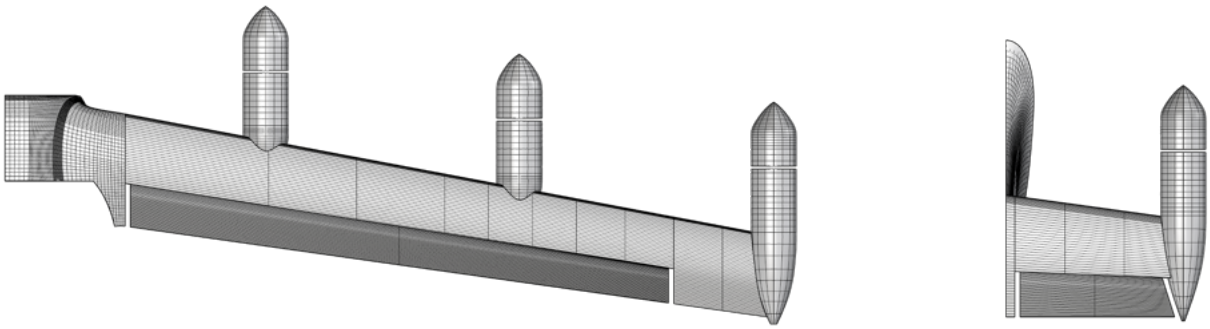

Figure 4: Control surfaces of the tiltwing vehicle: flaperon on the main wing (left) and elevator on the horizontal tail (right).

ume grids are then created using hyperbolic marching methods which extend the grid out to a fixed distance from the surface. Tight clustering in the normal direction near the wall is maintained to achieve sufficient boundary layer resolution in viscous flow computations. The normal grid spacing of all grids at the walls maintains $y^+ \leq 1$. Mesh orthogonality is maximized to provide better solution accuracy. NB volume grids are extended ensuring that the outer boundaries are outside the boundary layer. Uniformly spaced off-body Cartesian grids are utilized to resolve important flow features such as the wake region. Many Cartesian grids with successive levels of refinement based on proximity to the body are generated. Each Cartesian grid is twice as coarse as the previous level, and they expand the grid system to the far-field. The uniform spacing of the first OB grid level, which contains the resolved wake region, is 10 % of the blade tip chord length c_{tip}. Cartesian grids extend to the far-field boundary, which is 25 wing semispans away from the center of the vehicle in all directions.

Domain connectivity issues occur in the overset grid approach as grids arbitrarily overlap with each other, and some points of a grid might lie in the interior of a neighboring component. The domain connectivity step is robust and highly automated when using a trimmed approach. The X-ray hole cutting approach is used in this work. An X-ray object is created for every component of the geometry, i.e., blades, fuselage, landing gear, etc. The user has to supply the list of meshes that each X-ray object is allowed to cut and an offset distance with which to grow each hole away from the body. Hole cutting is required between components and with the OB Cartesian grids. This process is performed at each time step within the flow solver, allowing the rotating components to move relative to the fixed components.

CFD Flow Solver

OVERFLOW is a finite-difference CFD solver that uses the structured overset grid topology. It offers several inviscid flux algorithms, implicit numerical schemes, and turbulence models. For this work, the three-dimensional, time-dependent Reynolds-averaged Navier-Stokes (RANS) equations are solved in strong conservation form:

$$\frac{\partial \vec{\hat{q}}}{\partial t} + \frac{\partial\left(\vec{\hat{F}} - \vec{\hat{F}}_{\mathrm{v}}\right)}{\partial \xi} + \frac{\partial\left(\vec{\hat{G}} - \vec{\hat{G}}_{\mathrm{v}}\right)}{\partial \eta} + \frac{\partial\left(\vec{\hat{H}} - \vec{\hat{H}}_{\mathrm{v}}\right)}{\partial \zeta} = \vec{0}, \quad (1)$$

where ξ is the longitudinal coordinate, η is the circumferential coordinate, ζ is the nearly-normal coordinate. In equation (1), $\vec{\hat{q}} = \vec{q}/J$, being $\vec{q} = [\rho, \rho u, \rho v, \rho w, e]^{\mathsf{T}}$ the vector of conserved variables, and J the transformation Jacobian between generalized coordinates (ξ, η, ζ) and Cartesian coordinates (x, y, z). $\vec{\hat{F}}$, $\vec{\hat{G}}$, and $\vec{\hat{H}}$, as well as $\vec{\hat{F}}_{\mathrm{v}}$, $\vec{\hat{G}}_{\mathrm{v}}$, and $\vec{\hat{H}}_{\mathrm{v}}$ are related to the inviscid and viscous fluxes, respectively, by the same coordinate transformation.

The simulation is advanced in time using the 2$^{\mathrm{nd}}$-order accurate backward Euler method, where dual time-stepping is used to march in dual-time $\Delta\tau$ to steady-state. The physical time step Δt corresponds to 0.25° of proprotor rotation, together with up to 50 dual-time sub-iterations to achieve 3 orders of magnitude drop in sub-iteration residual. The inviscid flux vectors at the cell interfaces use 6$^{\mathrm{th}}$-order central differences and 5$^{\mathrm{th}}$-order artificial dissipation to damp out high-frequency errors, resulting in a 5$^{\mathrm{th}}$-order accurate discretization. The viscous terms are differenced to 2$^{\mathrm{nd}}$-order. The diagonalized form of the diagonally-dominant alternating direction implicit (DDADI) factored scheme (Ref. 23) is used to solve equation (1).

OVERFLOW currently includes algebraic, one-equation, and two-equation turbulence models, with the choice of hybrid Reynolds-averaged Navier-Stokes/large eddy simulation (RANS/LES) frameworks.

In this work, the one-equation Spalart-Allmaras model (Ref. 24) is used with the detached eddy simulation (DES) modification (Ref. 25). The DES approach introduces a limiter that switches between RANS and LES depending on the grid resolution. Near-wall regions are treated in RANS mode since turbulent scales are very small and need to be modeled; and the rest of the flow is treated in LES mode, where the largest turbulent scales are grid-resolved. The turbulence length scale d is replaced by $\bar{d}$:

$$\bar{d} = \min(d, C_{\mathrm{DES}}\Delta), \quad (2)$$

which is the minimum of the distance from the wall d and C_{DES} times the local grid spacing Δ, thus mitigating the problem of artificially large eddy viscosity. Excessive grid refinement can activate the DES limiter inside the boundary layer. In this case, the Reynolds stresses can become under-resolved which, in turn, can lead to grid-induced separation. The delayed detached eddy simulation (Ref. 26) is an extension of the DES concept that shields the boundary layer from the DES limiter, ensuring the RANS mode remains active. The wall-parallel grid spacing used in this study does not violate the hybrid-LES validity condition; thus, DES and DDES should give similar results. Nevertheless, all computations have been performed using the DDES model for both NB and OB grids.

Comprehensive Analysis

Structural dynamics and vehicle trim for the coupled calculations are performed using the comprehensive rotorcraft analysis code CAMRAD II . CAMRAD II performs an aeromechanics analysis of rotorcraft that incorporates a collection of computational models, including multibody dynamics, nonlinear finite elements, and rotorcraft aerodynamics. The trim task finds the equilibrium solution for a steady-state operating condition and produces the solution for performance, loads, and vibration. The aerodynamic model for the rotor blade is based on lifting-line theory, using two-dimensional airfoil characteristics and a vortex wake model. The aerodynamic properties of the airframe are defined in wind axes for three collocation points: the wing-body, horizontal tail, and vertical tail. CAMRAD II has undergone extensive correlation with performance and load measurements on rotorcraft.

Loose Coupling Methodology

The coupling interface between OVERFLOW/CAMRAD II was initially introduced in 2006 (Ref. 27). The methodology relies on a loose coupling and enables a modular approach where each code operates independently and communicates with the other through input/output files. The codes are coupled on a per revolution, periodic basis to calculate rotor airloads, and the exchange of information occurs at the end of each coupling cycle.

This work further extends the existing framework to update the computation of forces and moments acting on specific airframe components, such as the wing-body, horizontal tail, and vertical tail. The coupling procedure is illustrated in figure 5. Airframe and rotor trim occur simultaneously, although they are depicted separately for clarity. The coupling sequence advances as follows:

1. The simulation is initialized with a comprehensive analysis in CAMRAD II that results in a steady-state equilibrium solution for the vehicle. This analysis provides blade deflections, orientation angles, and control angles. The blade deflections are obtained through initial quarter chord motions as a function of the nondimensional radial coordinate r/R and azimuth angle ψ. The orientation angles include the pitch, yaw, and roll angles that define the position of the vehicle with respect to inertial axes. Lastly, control angles represent the deflection of the aerodynamic control surfaces.

2. These comprehensive analysis results are transferred to OVERFLOW. Blade motions are handled through aeroelastic grid deformation. Any blade surface grid point is transformed based on its position via two-dimensional

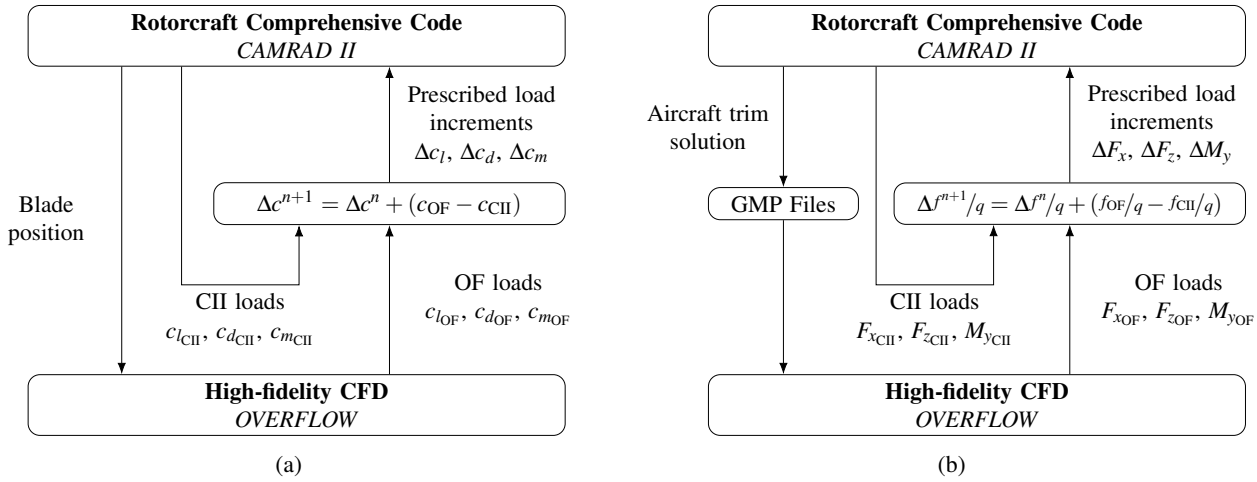

Figure 5: Flow diagram for CFD/comprehensive analysis loose coupling methodology: (a) rotor trim and (b) airframe trim.

interpolation of CAMRAD II motions. The six motions — three translations and three rotations— account for blade dynamics, elastics, and control inputs. Volume grids are then adjusted according to the new surface motions. Orientation and control angles determine the rigid body positions of the airframe and aerodynamic control surfaces. These are specified through geometry manipulation protocol (GMP) XML files. This study is concerned with longitudinal motion, so only the airframe pitch and tail elevator deflection are exchanged.

3. OVERFLOW is run with the prescribed motions for two to three rotor revolutions in the first coupling step. The CFD solution does not need to be converged at this point. For each blade, OVERFLOW outputs the normal force N', pitching moment M', and chord force C' as a function of r/R and ψ. Integrated airloads on specified components are also obtained thanks to the force and moment integration utility. The longitudinal airloads are horizontal force F_x, vertical force F_z, and pitch moment M_y.

4. The forces and moments used by CAMRAD II in the next iteration $n+1$ need to be corrected based on the most recent CFD solution. If the correction takes the form of an input increment, it reads:

$$\begin{aligned} \Delta c^{n+1} &= \Delta c^n + (c_{\mathrm{OF}} - c_{\mathrm{CII}}), \\ \frac{\Delta f^{n+1}}{q} &= \frac{\Delta f^n}{q} + \left(\frac{f_{\mathrm{OF}}}{q} - \frac{f_{\mathrm{CII}}}{q} \right), \end{aligned} \tag{3}$$

where c represents an arbitrary aerodynamic rotor coefficient and f an arbitrary airframe force/moment. Per its definition in the CAMRAD II inputs, the latter are non-dimensionalized with the dynamic pressure q. For each iteration, the increments are updated from the difference between the CFD loads and the total comprehensive analysis airloads, which include the increments from the preceding iteration. For the initial coupling cycle, the increments are the difference between CFD and the uncorrected comprehensive analysis airloads:

$$\begin{aligned} \Delta c^1 &= c_{\mathrm{OF}} - c_{\mathrm{CII}}, \\ \frac{\Delta f^1}{q} &= \frac{f_{\mathrm{OF}}}{q} - \frac{f_{\mathrm{CII}}}{q}. \end{aligned} \tag{4}$$

The sectional pitching moment $M^2 c_{\mathrm{m}}$, normal force $M^2 c_{\mathrm{n}}$, and chord force $M^2 c_{\mathrm{c}}$ coefficients are defined as:

$$\begin{aligned} M^2 c_{\mathrm{m}} &= \frac{M'}{\frac{1}{2}\rho a^2 c^2}, \\ M^2 c_{\mathrm{n}} &= \frac{N'}{\frac{1}{2}\rho a^2 c}, \\ M^2 c_{\mathrm{c}} &= \frac{C'}{\frac{1}{2}\rho a^2 c}. \end{aligned} \tag{5}$$

The aerodynamic properties of the airframe components in CAMRAD II are defined in wind axes by means of the lift L, drag D, and aerodynamic pitch moment $M_{y_{\mathrm{a}}}$. The horizontal force F_x, vertical force F_z, and pitch moment M_y, here expressed in body axes, are related to the former as:

$$\begin{aligned} F_x &= L\sin\alpha - D\cos\alpha, \\ F_z &= -L\cos\alpha - D\sin\alpha, \\ M_y &= M_{y_{\mathrm{a}}} + \left(\vec{r} \times \vec{F} \right) \cdot \vec{\hat{j}}. \end{aligned} \tag{6}$$

In the above equations, for each airframe component, α is the angle of attack, $\vec{r}$ a vector defining the collocation point position in body axes, and $\vec{F}$ the total force acting on it in body axes.

5. With the corrected loads, CAMRAD II is rerun to provide the trim solution.

6. Steps 2-5 are repeated every rotor revolution until convergence. Convergence is achieved when the orientation angles, control angles, and CFD aerodynamic forces do not change between iterations —within a small tolerance. In an iterative fashion, the comprehensive analysis airloads are replaced with the CFD airloads, resulting in a consistent coupled aerodynamic and structural solution.

RESULTS

The transition maneuver is the most critical flight phase of tiltwing aircraft. From hover to cruise, the proprotors must provide sufficient thrust to support the weight as they tilt and accelerate the vehicle to a condition where the wing provides sufficient lift. From cruise to hover, the same balance must be achieved in reverse. NASA's tiltwing operates with two control states based on the relative positioning of the wing to the fuselage. Within the range of wing tilt angles spanning from 90° to 20°, mean and differential collective control are utilized to trim the vertical force and the pitch moment, whereas the pitch attitude is the primary variable for the horizontal force trim. For wing tilt angles ranging between 20° and 0°, control actuators include rotor collective for horizontal force, pitch attitude for vertical force, and elevator deflection for pitch moment.

Gladfelter et al. (Ref. 28) defined a transition corridor for NASA's tiltwing vehicle using FLIGHTLAB (Ref. 29) simulation results. The trim characteristics were obtained for a sweep of airspeeds with wing tilt angle and flap deflection schedules originating from NDARC (Ref. 30) modeling. Figure 6 illustrates the relative positioning of the wing to the fuselage as a function of the forward flight velocity. In this study, four operating conditions along this transition corridor —labeled in figure 6— have been simulated by loosely coupling the OVERFLOW and CAMRAD II codes. These points have been chosen as representative conditions of the two control states. Each point has been treated as steady-level flight, neglecting the dynamic effects of changing the flight condition. Table 2 summarizes the fixed input parameters for each simulation. All simulations are carried out in standard atmosphere at an altitude of $h = 6000\,\text{ft}$.

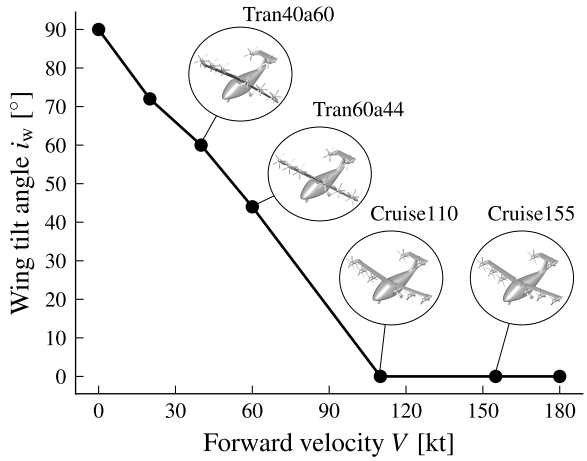

Figure 6: Nominal wing tilt angle as a function of forward flight velocity in the transition corridor.

Computations have been performed using 2520 cores on NASA's supercomputers Pleiades, Electra, and Aitken located at the NASA Advanced Supercomputing (NAS) Division. The computational cost per revolution was 7-9 h, which corresponds to 1440 physical time steps at 0.25°. A typical job requires approximately 240 h of wall-clock time for convergence.

Table 2: Transition corridor operating conditions.

	Tran40a60	Tran60a44	Cruise110	Cruise155
Forward velocity V [kt]	40	60	110	155
Wing tilt angle i_w [°]	60	44	0	0
Flap deflection δ_f [°]	0	60	20	0
Rotor tip speed V_{tip} [ft/s]	550	550	300	300

In the subsequent sections, the results of the simulations are discussed in depth. A complete description is given for the first cases of conversion mode and airplane mode, whereas for the second cases, the discussion will focus on the differences with the former.

Transition mode at 60°, Tran40a60

This configuration represents an early transition stage, in which the vehicle has already gained some forward momentum. The flight speed is $V = 40\,\text{kt}$ and the wing is rotated by $i_w = 60°$.

Figure 7 shows the instantaneous iso-surfaces of Q-criterion colored by nondimensional vorticity magnitude and serves as a basis for analyzing the wake structure. To a certain extent, the aerodynamics are similar to those of forward flight in a conventional helicopter. The flow about each proprotor is characterized by lateral asymmetry and is influenced by the vortex dynamics. Blade tip vortices are convected rearward by the freestream velocity component parallel to the disk, as well as downward by the normal velocity component. Thus the wake nominal trajectory consists of skewed, interlocking helices. Due to the relatively low advance ratio $\mu \approx 0.12$ and high incidence $i_w = 60°$, tip vortices are carried downward at a much faster rate. In the close-up view of the middle and outboard wing proprotors, blades are seen to slice through the tip vortices from the preceding blade, particularly in the front section of the proprotor disk. As the blade traverses these azimuth positions, the tip vortex originating from the preceding blade progressively sweeps radially along the blade span, affecting more inboard positions. In the same image, rotor-on-rotor interactions can be observed in regions of the wingspan located where proprotor edges are near each other, when a retreating blade passes beneath the advancing blade of the neighboring proprotor. In this scenario, a complex interaction that affects the blade loading occurs involving three vortices: those shed from the retreating blade, the advancing blade, and the preceding advancing blade. For simplicity, they will be referred to as R1, A1, and A5, respectively. The corresponding blades from which they are shed are indicated in figure 7c. The swirling motion of the vortices directs the flow towards the opposite proprotor. Initially, A5 is influenced by R1, causing it to deflect upwards and to the left. Then, the induced velocity from A1 pushes A5 downward and to the left. The influence of A1 is stronger due to a larger pressure differential in the advancing blade, forcing A5 to remain close to the proprotor plane. Transverse vortical structures subsequently appear between A5 and R1, possibly caused by the relatively intense stretching between these counter-rotating vortices.

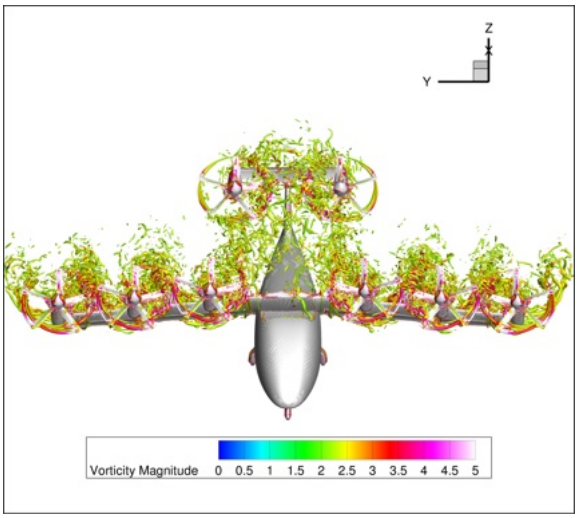

(a)

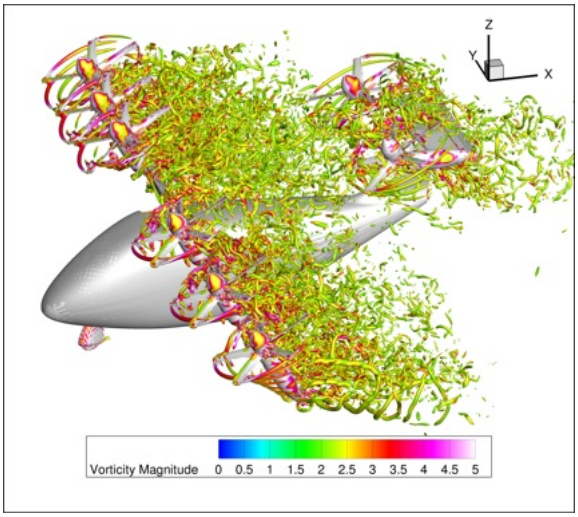

(b)

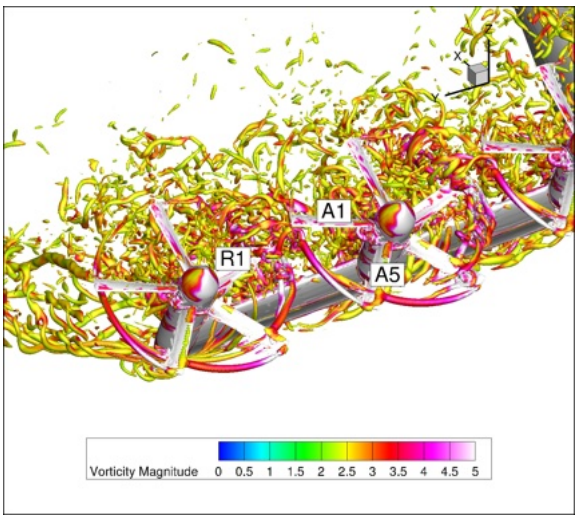

(c)

Figure 7: Snapshot in time of the iso-surfaces of Q-criterion colored with nondimensional vorticity magnitude for Tran40a60: (a) front view, (b) lateral view, and (c) close-up view of wing proprotor interactions.

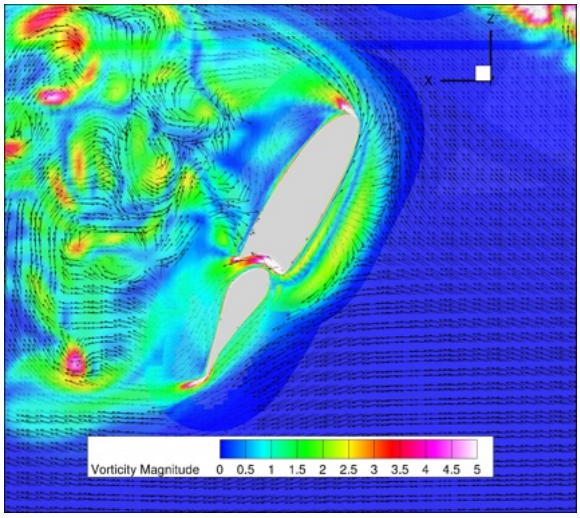

(a)

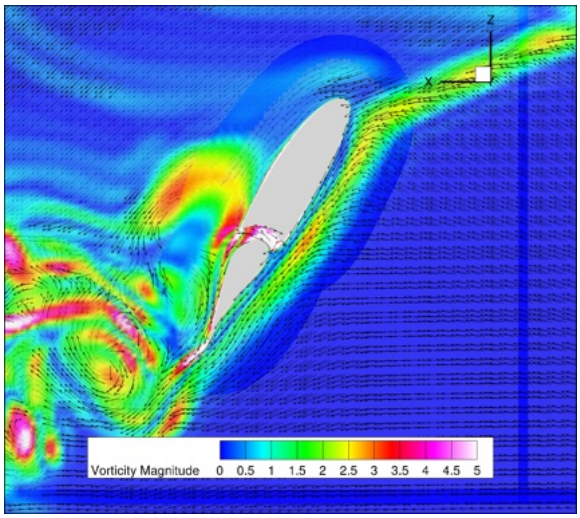

(b)

Figure 8: Snapshot in time of the contour of the nondimensional vorticity magnitude field for Tran40a60 at two wingspan sections: (a) $2y/b = 0.525$ and (b) $2y/b = 0.75$. Arrows indicate the local direction of the flow.

Several other aerodynamic interactions between various components of the vehicle can significantly affect flight dynamics and performance. For example, the proprotors increase the static pressure on the wing because of the energy contained in the wake, and the impingement of tip vortices on the wing surface produces unsteady pressure changes. The blowing and swirling effects, however, may be exploited to delay wing stall. The proprotors are staggered longitudinally across the wing to provide a uniform blowing, aiming to reduce flow separation during transition flight. The proprotor swirl locally affects the angle of attack of the wing α_w. This influence has opposing effects in the advancing and retreating regions. On the advancing side, the proprotors generate a downwash that decreases α_w. This interaction is favorable in transition as it helps maintain the flow attached despite the high incidence. On the retreating side, the proprotors induce an upwash that amplifies the adverse effects of the high angle of incidence,

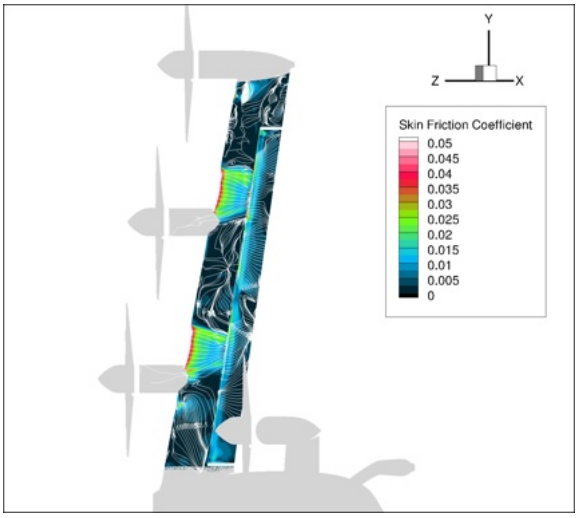

Figure 9: Snapshot in time of the streamtraces and the skin friction coefficient distribution on the upper surface of the wing for Tran40a60.

locally increasing α_w and triggering flow separation. Both effects are illustrated in figure 8. The figure shows two slices taken at cross-sections of the wing located behind the advancing and retreating sides of the middle proprotor. Note that in both cases, high pressure air flowing through the flap slot helps in maintaining the flow attached to the flap surface. In order to analyze the extent of the separated flow regions, figure 9 shows the surface streamtraces and skin friction coefficient distribution on the upper surface of the wing. The flow is attached at wingspan sections influenced by the proprotor downwash up to approximately $r/R = 0.75$. Between $0.75 < r/R < 1$, the separated flow is likely caused by the ascending blade of the neighboring proprotor, which is located closer to the wing. To mitigate this problem, other tiltwing designs, such as the XC-142A (Ref. 31), placed leading-edge slats along the wing behind the upgoing propeller blades. As observed in the slices, the flow remains attached over a great portion of the flap.

The tail proprotors partially operate within the separated flow from the wing, which creates unsteadiness and reduces their efficiency. There are no evident mutual interactions observed between these proprotors, given their placement at a greater distance from each other.

In such a rotor-borne regime, the control of the vehicle involves utilizing front rotor and rear rotor collective control θ_0 to trim the vertical force and pitch moment, and pitch attitude Θ to trim the horizontal force. The time history of these variables is plotted in figure 10. In the first 10 OVERFLOW-CAMRAD II coupling cycles, the airframe pitch undergoes a rapid change, but it stabilizes after about 15 cycles. The initial solution is obtained with the uncorrected aerodynamics analysis from CAMRAD II. In this case, lift stall is modeled by truncating the angle of attack to a maximum of $\alpha_{max} = 20°$. For this flight condition, the wing incidence alone exceeds this value, rendering lift and drag predictions highly inaccurate. As the coupling advances and the comprehensive airloads are replaced by the CFD values, the airframe pitch reaches a quasi-steady

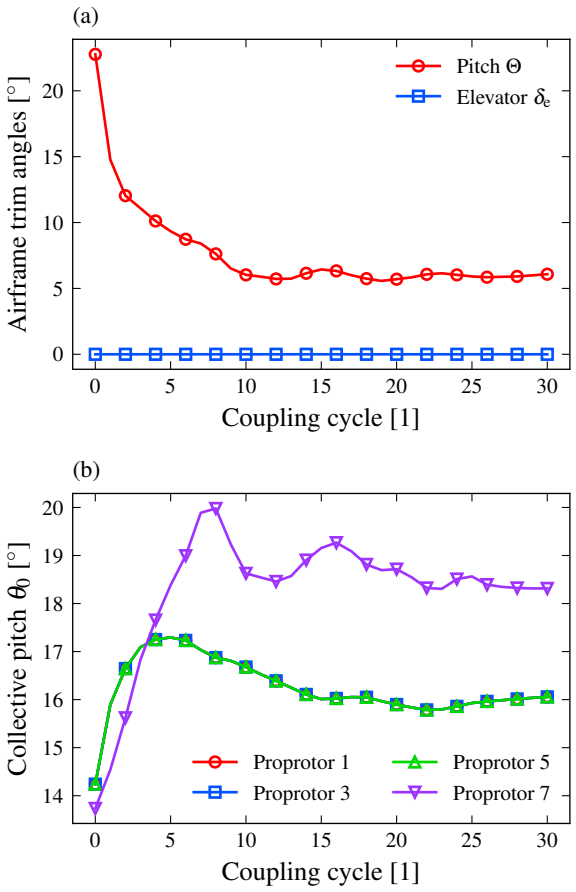

Figure 10: Convergence history of the trim angles for Tran40a60: (a) airframe pitch Θ and elevator deflection δ_e, and (b) rotor collective pitch θ_0. The final trimmed values are $\Theta = 6.1°$, $\theta_{0_{1,3,5}} = 16.1°$, and $\theta_{0_7} = 18.3°$.

state. The rotor collective pitch adjustments initially respond to changes in the vehicle's attitude. The input decks enforce an equal collective trim for the wing proprotors, different from that of the tail proprotors, in order to generate the required forces for longitudinal trim. Compared to tail proprotors (proprotor 7), the trim convergence of wing proprotors (proprotors 1, 3, and 5) is observed to be smoother. This is possibly due to unsteady vortex shedding from the wing inducing oscillatory loading on the tail. Initially, a coupling strategy of exchanging time-averaged loads every rotor revolution was employed, but it resulted in a poor convergence rate due to the flow unsteadiness. Eventually, adopting an average window of five rotor revolutions proved more efficient, while still performing the coupling every rotor revolution. Given the complexity of the simulation, the rotor collective pitch was considered sufficiently converged after 25 coupling cycles. The elevator remained undeflected for this control state.

Further exploring the trim solution, figure 11 presents a breakdown of the longitudinal aerodynamic and inertial forces in body axes subdivided into: (a) horizontal force F_x, (b) vertical force F_z, and (c) pitch moment M_y. To evaluate the aerodynamic forces, the vehicle is broken down into five components: tail proprotors, wing proprotors, vertical tail, horizontal tail,

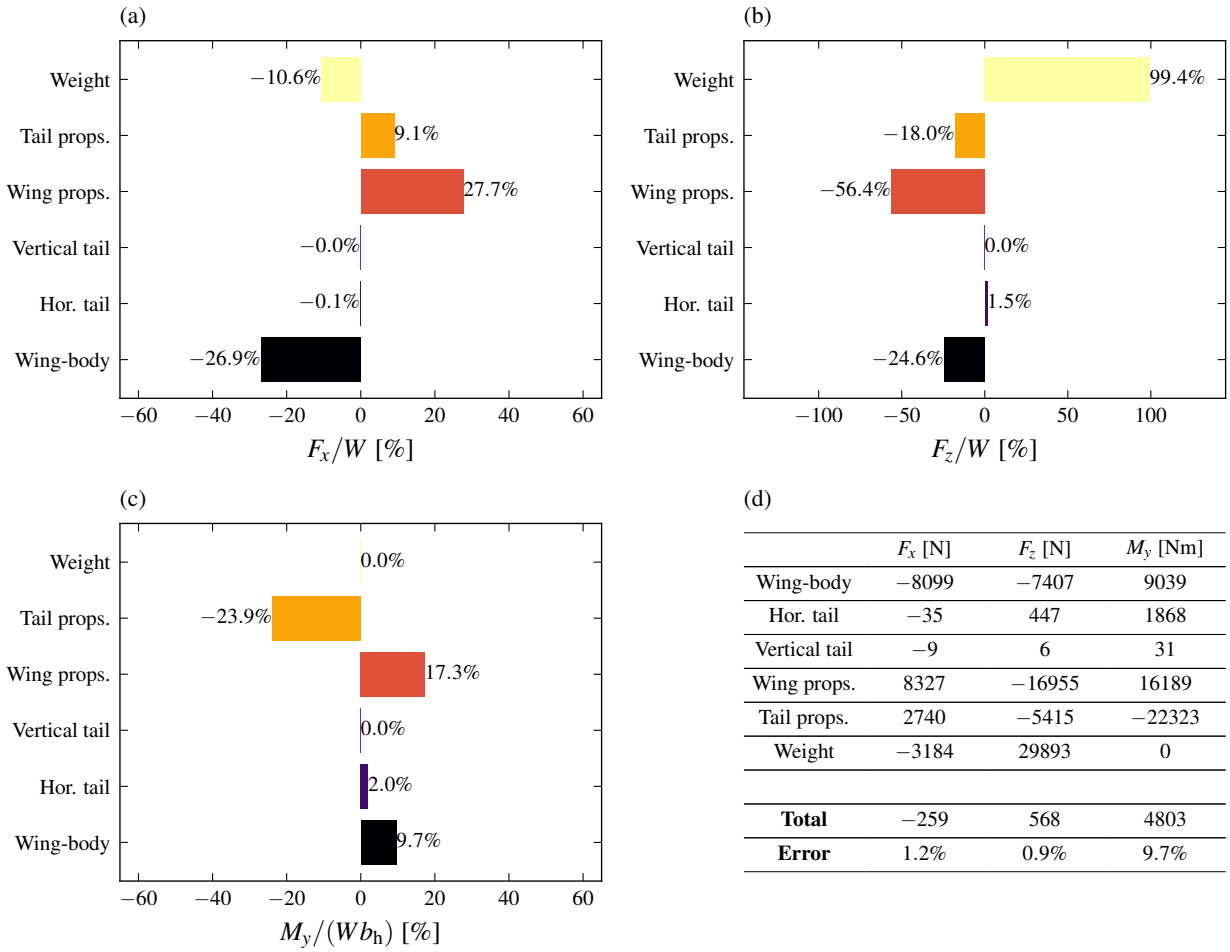

(d)

	F_x [N]	F_z [N]	M_y [Nm]
Wing-body	−8099	−7407	9039
Hor. tail	−35	447	1868
Vertical tail	−9	6	31
Wing props.	8327	−16955	16189
Tail props.	2740	−5415	−22323
Weight	−3184	29893	0
Total	−259	568	4803
Error	1.2%	0.9%	9.7%

Figure 11: Balance of inertial and aerodynamic forces for Tran40a60 in body axes: (a) horizontal force F_x, (b) vertical force F_z, (c) pitch moment M_y, and (d) trim solution. The horizontal and vertical forces are expressed as a percentage of the vehicle's weight. The pitch moment is expressed as a percentage of the vehicle's weight times the horizontal tail span. The sign of the percentage corresponds to the sign of the force.

and wing-body. The latter includes the fuselage, wing, and landing gear. The horizontal and vertical forces are expressed as a percentage of the vehicle's weight. The pitch moment is expressed as a percentage of the vehicle's weight times the horizontal tail span. For supplementary reference, a table with the values used to produce the bar plots is provided in subfigure (d). The error is calculated as a percentage of the sum of the absolute values of the total force along each axis. Several observations can be made:

- Along the x-axis, the horizontal force equilibrium is established between the gravity component (−10.6 %) and the aerodynamic action on the wing-body (−26.9 %) in the negative direction of the axis, and the aerodynamic action on the tail proprotors (9.1 %) and wing proprotors (27.7 %) in the positive direction of the axis. The notable contribution of the wing-body is due to the wing being stalled, thus generating significant drag.
- Along the z-axis, the fundamental contributions are due to the gravity component (99.4 %), tail proprotors (−18 %), wing proprotors (−56.4 %), and wing-body (−24.6 %).
- Along the y-axis, the wing proprotors (17.3 %), wing-body (9.7 %), and to a lesser degree, horizontal tail (2 %) generate nose-up pitch moments and the tail proprotors (−23.9 %) produce a nose-down moment. Note that for this trim target, the error is close to 10 %. This error is caused by the unsteady nature of the case which hinders the convergence of the coupling algorithm on the pitch axis. Using a longer averaging time per cycle is a possible improvement that is left for future work, as the error is deemed acceptable for the purpose of the present analysis.

To investigate the blade loading distribution, figures 12 and 13 depict contour maps of the blade section normal force coefficient $M^2 c_n$ and pitch moment coefficient $M^2 c_m$. The azimuth angle ψ is measured in shaft axes, positive in the direction of rotation, and divides the proprotor disk into four quadrants of $\psi = 90°$ each. Due to the symmetric arrangement of the proprotors, only those located on the right-side are plotted. In figure 12, the maximum $M^2 c_n$ for proprotors 1, 3, and 5 appears in the outboard regions $0.8 < r/R < 1$ on the advancing side of the disk. The strong radial variation of the normal

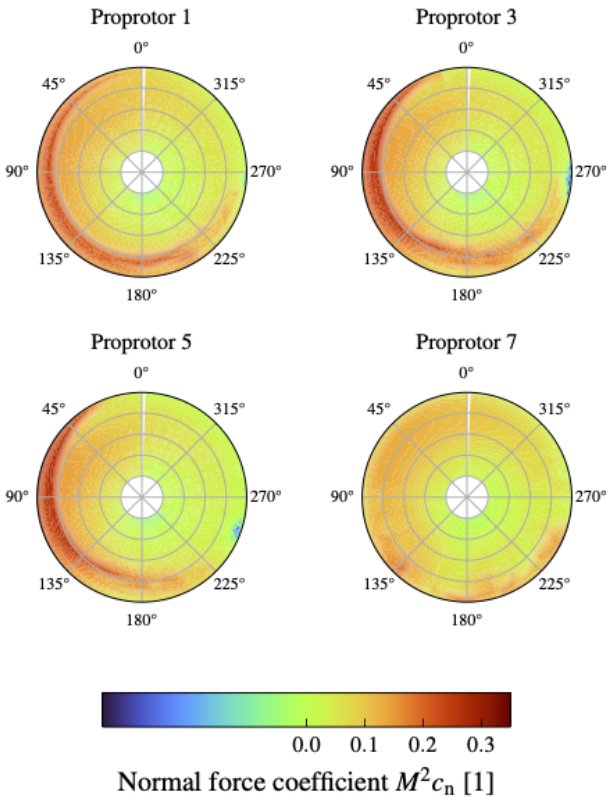

Figure 12: Sectional normal force coefficient M^2c_n distribution for Tran40a60.

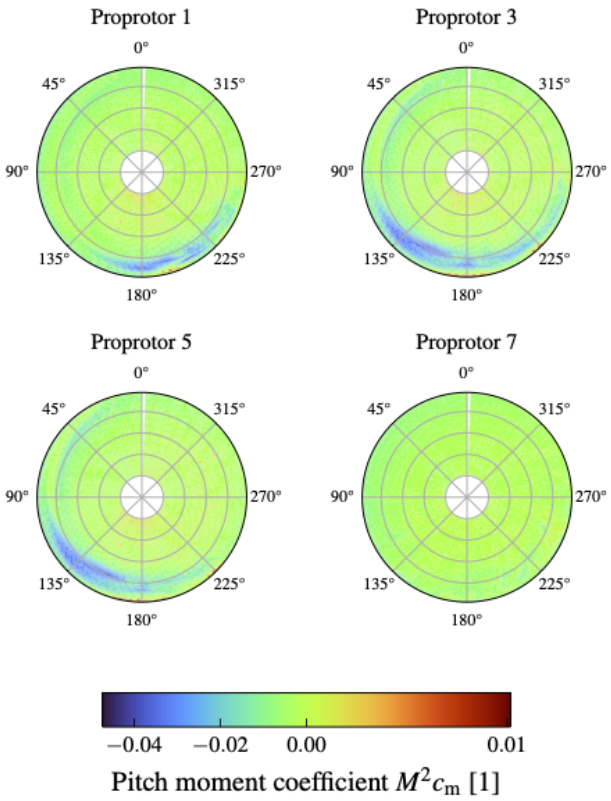

Figure 13: Sectional pitch moment coefficient M^2c_m distribution for Tran40a60.

force near the tip can be attributed to the proximity of the vortices. Initially, the tip vortices affect the outermost sections of the following blade, as seen in the first quadrant. Then, the contraction of the slipstream and the incident flow displace the vortices towards inner radial positions, reaching into the midspan region of the blade, as seen in the second and third quadrants. The most pronounced radial changes occur in the range $15° < \psi < 225°$, although the azimuthal extent slightly varies for each proprotor. For example, mutual interactions between proprotors 1 and 3, as well as between proprotors 3 and 5, extend this azimuthal range to $\psi \approx 270°$ for the former. These same interactions are responsible for sharper force peaks observed on the advancing side of proprotors 3 and 5. As discussed in figure 7, the vortex shed by the retreating blade induces an upwash that increases the local angle of attack in that portion of the disk. In the vicinity of $\psi = 270°$, M^2c_n becomes slightly negative for proprotors 3 and 5. Nevertheless, these values are very close to zero. The wake of wing proprotors and separated flow from the wing impinges on the lower portion of the disk of tail proprotors. This produces impulsive changes in M^2c_n, as seen in the contour plot of proprotor 7. Note that the strong radial variations on the advancing side observed for wing proprotors are not observed for tail proprotors. This can be for two reasons. Firstly, tail proprotors operate at a higher collective setting —see figure 10— with a possibly higher induced velocity that could push the vortices downward more rapidly. Secondly, the incoming flow is not obstructed by the wing, which in the vicinity of wing proprotors causes an upwards deviation, narrowing the separation of the vortices.

In figure 13, M^2c_m experiences a notable drop for $0.8 < r/R < 1$ in the front portion of the disk for proprotors 1, 3, and 5. This corresponds to a pitch down moment in areas that partially overlap with those of change of the normal force. For proprotor 1, the pitch moment drop begins when the blades transition from the second to third quadrant. For proprotors 3 and 5, the minimum moment appears already in the second quadrant. These differences may be attributed to the interference from the adjacent proprotor on the advancing side, which does not affect proprotor 1, located at the wingtip. It was observed that the leading edge suction peak was greater for proprotors 3 and 5 in those positions. However, dedicated analyses of rotor-on-rotor interactions are necessary to confirm this hypothesis. The front portion of the disk, around $\psi = 180°$, exhibits unsteady fluctuations, especially in the innermost regions, where pitch up moments are observed. In the case of proprotor 7, the distribution pattern of M^2c_m is fairly uniform. As discussed, tail proprotors experience weaker interactions with self-generated vortices, and they are more widely spaced than wing proprotors, which minimizes mutual interferences. The separated wake from upstream components seems to have minimal effect on the sectional pitch moment.

Figure 14 shows the time-averaged elemental forces $\overline{M^2c_n}$ and $\overline{M^2c_m}$ over the period of one rotor revolution versus the nondimensional radial coordinate r/R. The normal force increases along the blade span with a peak at $0.85 < r/R < 0.9$ induced by the interaction with the tip vortex of the preceding blade.

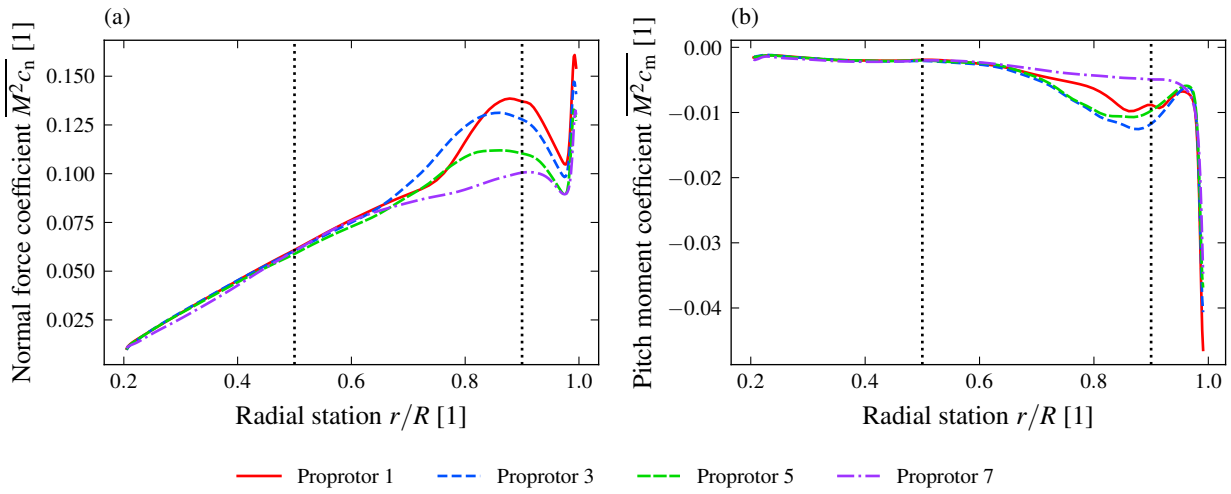

Figure 14: Radial distribution of airloads for Tran40a60: (a) normal force coefficient $M^2 c_n$ and (b) pitch moment coefficient $M^2 c_m$. The radial stations $r/R = 0.5$ and $r/R = 0.9$ are marked with dashed lines to indicate the mean value used to normalize the azimuthal distributions.

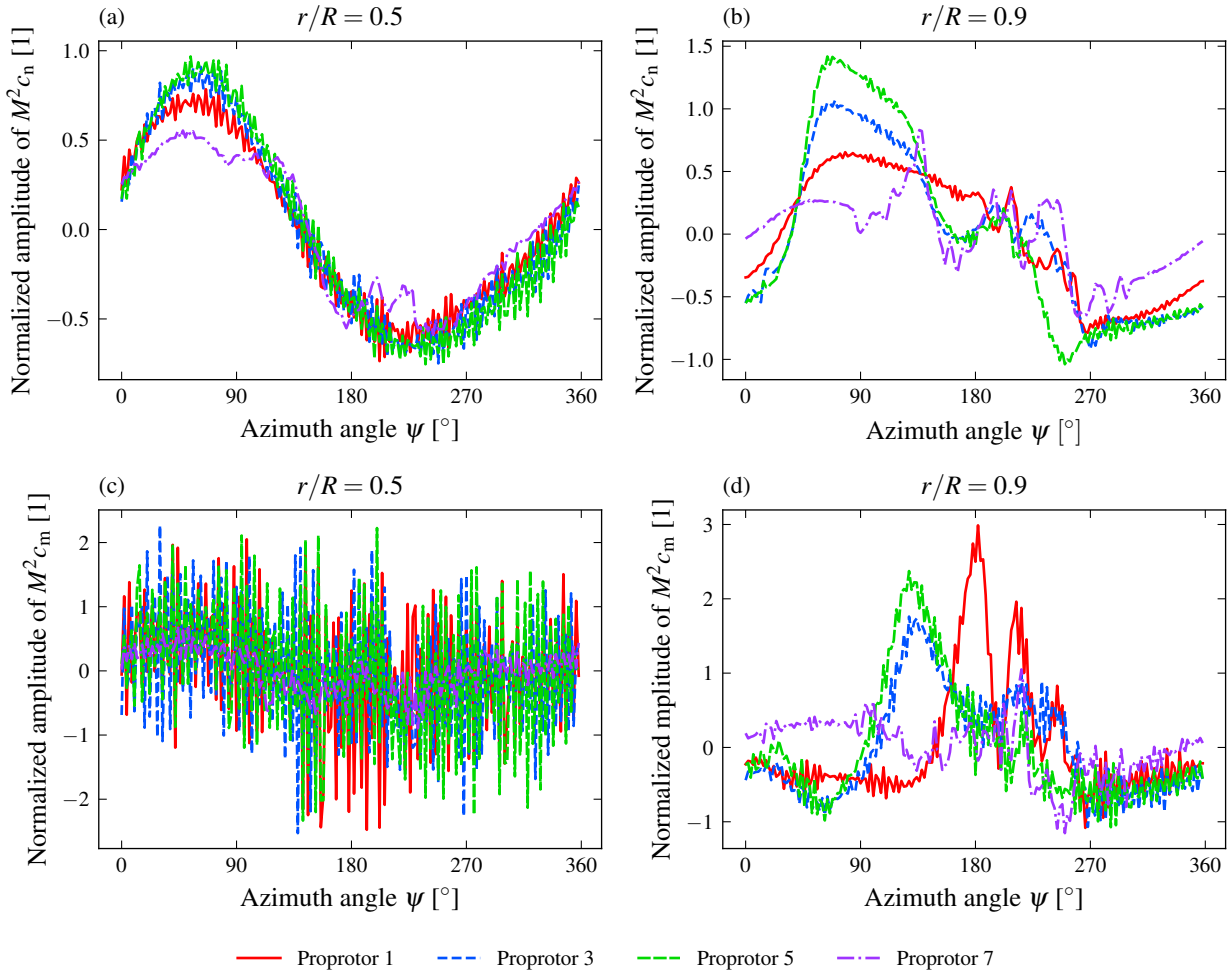

Figure 15: Azimuthal distribution of the fluctuations of the airloads for Tran40a60: (a) normal force coefficient $M^2 c_n$ at $r/R = 0.5$, (b) normal force coefficient $M^2 c_n$ at $r/R = 0.9$, (c) pitch moment coefficient $M^2 c_m$ at $r/R = 0.5$, and (d) pitch moment coefficient $M^2 c_m$ at $r/R = 0.9$. The mean is removed and the fluctuations are normalized by the mean value at the corresponding radial station.

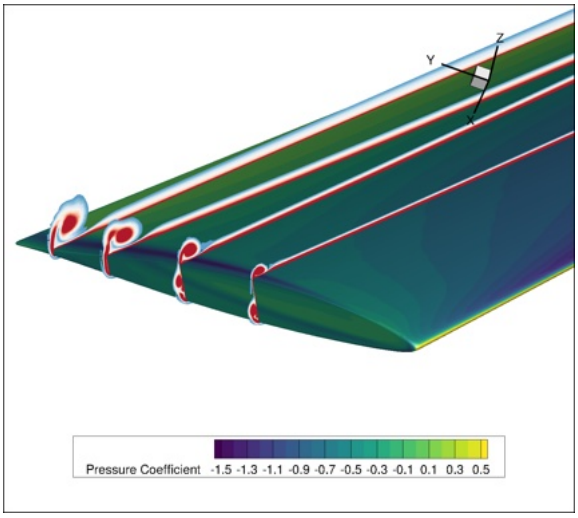

Figure 16: Close-up view of the formation of the blade tip vortex. Red areas indicate regions of high vorticity magnitude.

Note that weaker interactions for proprotor 7 result in a more modest peak. In sections $0.95 < r/R < 1$, the normal force experiences a sudden increase. This is believed to be caused by the development of the tip vortex on the upper surface of the blade. The core of the vortex induces a strong low-pressure region that extends through a fine strip in the chordwise direction —see figure 16. The pitch moment remains relatively constant for $r/R < 0.6$, with a peak in pitch down moment observed in the outer radial stations. As hinted by the rotor maps, the change of pitch moment is stronger for proprotors 3 and 5. Again, in sections $0.95 < r/R < 1$, the very strong pitch down moment is thought to be caused by tip vortex core influence.

To conclude the blade loading analysis, the amplitude of the oscillations of M^2c_n and M^2c_m —mean removed— are plotted against the azimuth angle ψ for two radial stations at $r/R = 0.5$ and $r/R = 0.9$ in figure 15. For each section, the amplitude is normalized by the mean value of the correspondent coefficient. Some observed features are:

- At the midspan section $r/R = 0.5$, the normal force is quasi-periodic around the azimuth. The fluctuations are comparable to the mean interaction, with half-peak amplitudes between 50 % to 100 % of the mean value. The maximum M^2c_n appears shortly before $\psi = 90°$, where the influence of the vortex is stronger. The pitch moment, as shown in figure 13, is highly unsteady for proprotors 1, 3, and 5. The oscillations deviate up to 200 % of the mean. These loads will be transmitted to the proprotor support structure as bending and twisting moments, thereby creating vibrations.

- At the outboard section $r/R = 0.9$, the behavior of the loads is more influenced by the vortices. For M^2c_n, this influence is stronger on the advancing side, roughly at $\psi = 70°$. The half-peak amplitude deviates approximately by 50 %, 100 %, and 150 % from the mean for proprotors 1, 3, and 5, respectively. It is worth noting that the mean values vary in the opposite direction, implying that the actual instantaneous loads are similar. For proprotor 7, interactions with the wake cause fluctuations comparable to the mean for azimuths between $135° < \psi < 270°$. In contrast, peaks of M^2c_m occur slightly later and are concentrated over the front portion of the disk, between $90° < \psi < 225°$. Fluctuations are larger than the mean, especially for wing proprotors, where the half-peak amplitude ranges from 200 % to 300 % of the mean.

Transition mode at 44°, Tran60a44

As the transition maneuver continues, the vehicle gains horizontal speed and the wing tilts down. This flight condition is defined by a forward velocity of $V = 60$ kt and a wing tilt angle of $i_\mathrm{w} = 44°$.

Figure 17 offers a visual representation of the wake structure through iso-surfaces of Q-criterion colored by nondimensional vorticity magnitude. The proprotor wake geometry shows characteristics akin to the wakes of a conventional helicopter during both forward and axial flight conditions. The vortices fundamentally trace out helices —similar to axial flight— with a cycloidal pattern —similar to forward flight. The skewness is less pronounced than the wake of a helicopter in forward flight because of the comparable axial and in-plane velocity components relative to the proprotor disks. Since each vortex is more widely spaced along the axial direction, they do not coil into a pair of super vortices at the edges of the wingtip proprotors. By the same token, their influence on the rotors is expected to be weaker. In the close-up view of the proprotors, none is seen slicing through the vortices. However, intense vortex stretching is seen at the gap between the edges of adjacent proprotors because of the close proximity of counter-rotating vortices. Substantial bluff body shedding is observed from the wing due to the high incidence $i_\mathrm{w} = 44°$ and flap deflection $\delta_\mathrm{f} = 60°$. The resulting separated flow interacts with the tail proprotors at the lower blade positions.

To investigate the slipstream effect on the wing, figure 18 shows two cross-sections of the flowfield at wingspan sections located behind the middle proprotor, $2y/b = 0.525$ and $2y/b = 0.75$. The slices are flooded with the nondimensional vorticity magnitude field and the local flow direction is indicated by arrow vectors. As seen in Tran40a60, the rotational motion of the blade can promote unfavorable flow separation. In a similar fashion, at $2y/b = 0.525$, located behind the retreating side of the proprotor, the combined effect of induced upwash and high incidence angles leads to significant flow separation from the wing. At $2y/b = 0.75$, situated behind the advancing side of the proprotor, the downwash and axial blowing delay flow separation on the upper surface. However, this delaying effect appears to be less effective than that of Tran40a60. In this case, the flap setting forces the high pressure air on the lower surface to flow through the slot into the upper surface. This blowing in the perpendicular direction highly energizes the flow, resulting in largely separated flow from the flap, and in an area of recirculation that roughly extends from 25 % to 60 % of the wing chord. The regions of

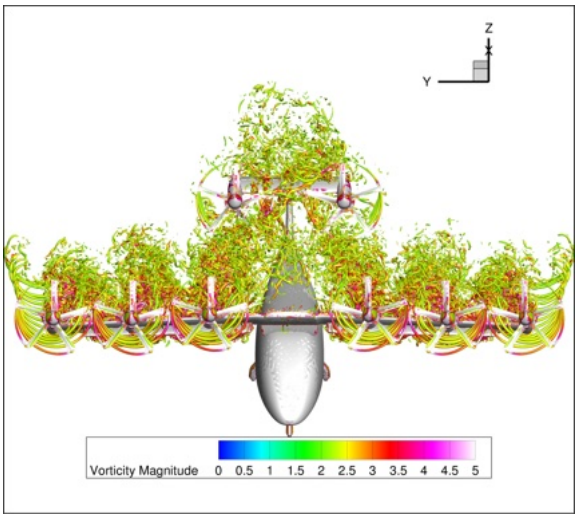

(a)

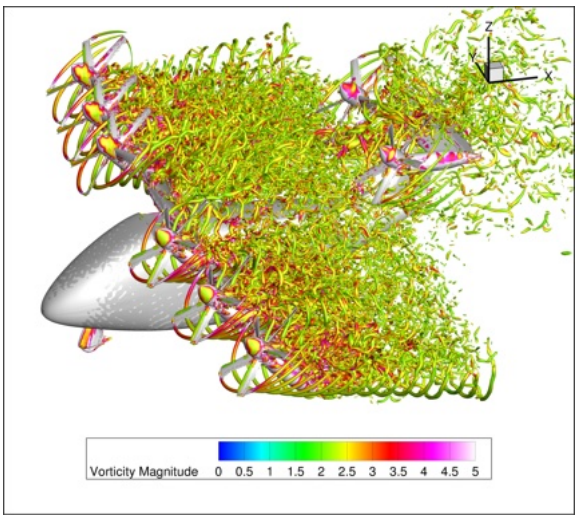

(b)

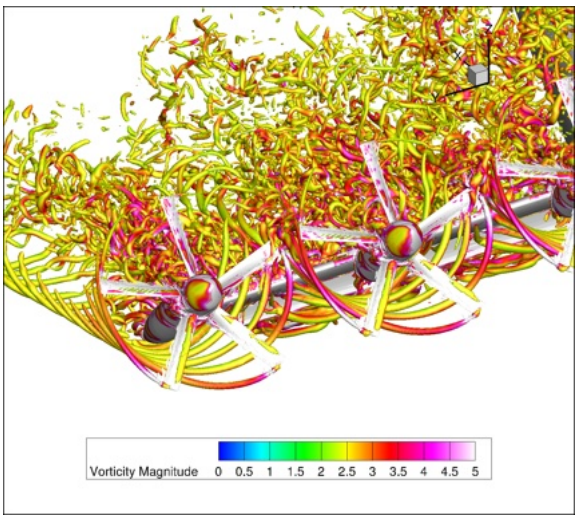

(c)

Figure 17: Snapshot in time of the iso-surfaces of Q-criterion colored with nondimensional vorticity magnitude for Tran60a44: (a) front view, (b) lateral view, and (c) close-up view of wing proprotor interactions.

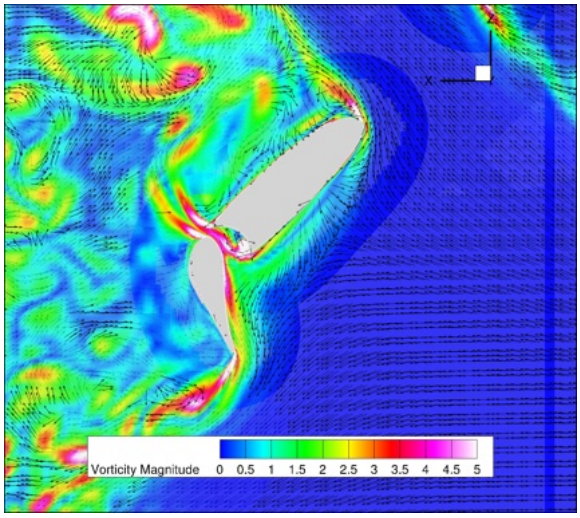

(a)

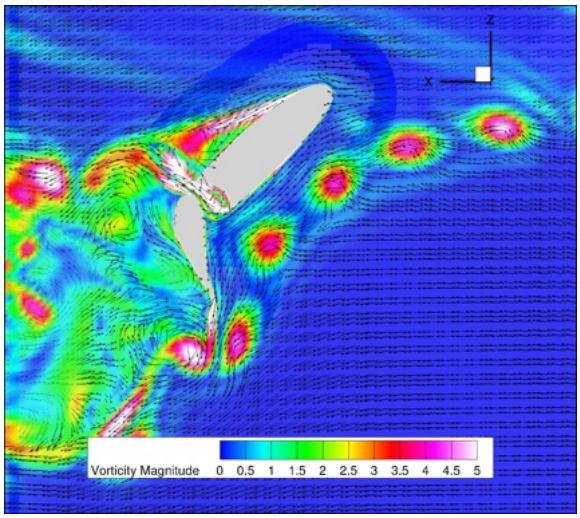

(b)

Figure 18: Snapshot in time of the contour of the nondimensional vorticity magnitude field for Tran60a44 at two wingspan sections: (a) $2y/b = 0.525$ and (b) $2y/b = 0.75$. Arrows indicate the local direction of the flow.

separated flow are visualized in figure 19. The figure shows the distribution of surface streamlines and skin friction coefficient on the upper surface of the wing. The areas benefiting from the downwash produced by the proprotors are considerably smaller than those of Tran40a60. The flow over the wing is highly unsteady, characterized by extensive areas of crossflow and reverse flow. It should be noted that the inclusion of the flap in this work primarily serves trim purposes, and a slotted flap design was chosen to facilitate mesh generation. Other flap designs are likely to provide superior aerodynamic performance in terms of mitigating flow separation under high angle of attack conditions.

Figure 20 shows the convergence history of pitch attitude Θ and rotor collective pitch θ_0. Similar to the previous flight condition, there is a marked change in the trim variables during the initial iteration cycles. This is again attributed to an inaccurate modeling of aerodynamic stall in CAMRAD II. The results sta-

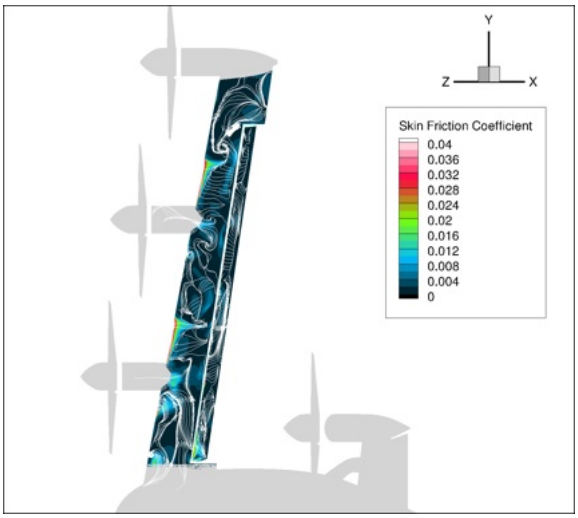

Figure 19: Snapshot in time of the streamtraces and the skin friction coefficient distribution on the upper surface of the wing for Tran60a44.

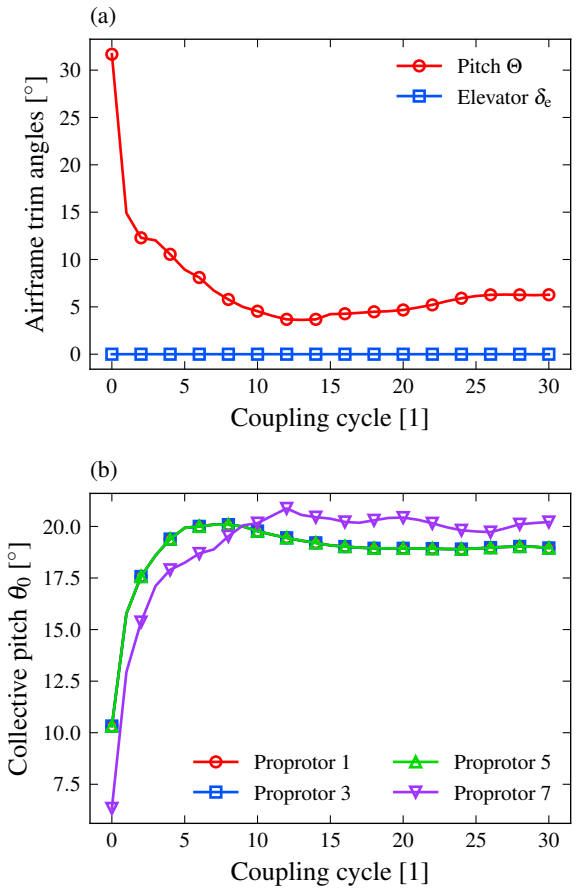

Figure 20: Convergence history of the trim angles for Tran60a44: (a) airframe pitch Θ and elevator deflection δ_e, and (b) rotor collective pitch θ_0. The final trimmed values are $\Theta = 6.3°$, $\theta_{0_{1,3,5}} = 19°$, and $\theta_{0_7} = 20.2°$.

bilize after 15 OVERFLOW-CAMRAD II coupling cycles and are considered converged after 25 cycles. The pitch is similar to the previous condition. In this case, the difference in trim values between the rotor collective pitch of wing proprotors and tail proprotors diminishes.

Figure 21 illustrates the breakdown of each component's contribution to the generation of inertial and aerodynamic actions on the vehicle, with values expressed in body axes. In the following discussion, some considerations are taken into account to simplify the analysis of this condition: (1) thrust is the main aerodynamic force acting on the proprotors, as it is one order of magnitude higher than drag; (2) for the wing-body component, both lift and drag are comparable in magnitude because the wing is stalled. Hence, since the pitch angle is small, drag will be referred to as the primary component in the horizontal direction and lift as the primary component in the vertical direction. It is important to note that the values presented in the table are a combination of both, according to equation (6). The trim state is detailed below:

- Along the x-axis, the gravity component (-10.9 %) and the aerodynamic action on the wing-body (-41.1 %) are counteracted by the aerodynamic actions on the wing proprotors (40.6 %) and tail proprotors (11.1 %). When the wing tilts down, the projection of the thrust vector onto the horizontal axis increases. However, the thrust magnitude also changes to adapt to the new trim condition. In comparison to Tran40a60, the increase in horizontal force is more significant for wing proprotors (46 %) than for tail proprotors (21 %). Given that both tilt by the same amount, this means that the amount of thrust produced by the tail proprotors has to decrease. For the wing-body, the horizontal force increases by 52 % in the negative direction of the axis, mainly due to the increased separated flow from the wing. The gravitational force component remains nearly unchanged since the pitch attitude is similar.

- Along the z-axis, the gravity component (99.4 %) is primarily balanced by the aerodynamic action on the wing proprotors (-48.9 %), wing-body (-35.0 %), and tail proprotors (-12.7 %). In this case, tilting down the wing reduces the projection of the thrust vector onto the vertical axis. In comparison to Tran40a60, the absolute contribution of the wing proprotors decreases by 13 % while that of the tail proprotors decreases by 29 %. For the wing-body, the combined effect of reducing the incidence and deploying the flap results in a 42 % increase in lift. Again, the weight contribution remains essentially the same.

- Along the y-axis, the pitch moment equilibrium is established between the nose-up moments of the wing proprotors (12.1 %) and wing-body (13.5 %), and the nose-down moments of the tail proprotors (-20.1 %) and horizontal tail (-1.9 %). Note that the pitch moment trim results in a 7.6 % error. This is considered acceptable given the unsteady nature of transition flight.

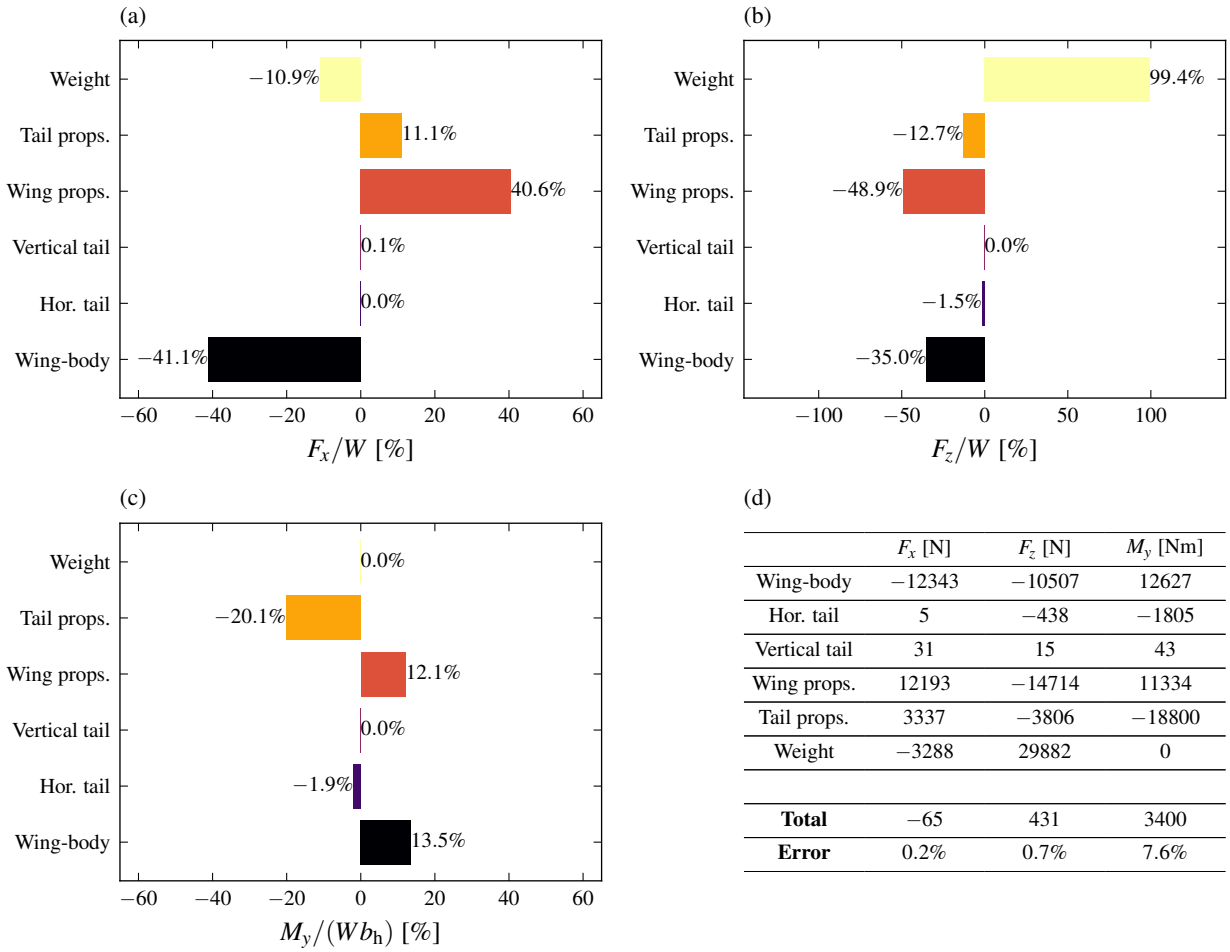

(d)

	F_x [N]	F_z [N]	M_y [Nm]
Wing-body	−12343	−10507	12627
Hor. tail	5	−438	−1805
Vertical tail	31	15	43
Wing props.	12193	−14714	11334
Tail props.	3337	−3806	−18800
Weight	−3288	29882	0
Total	−65	431	3400
Error	0.2%	0.7%	7.6%

Figure 21: Balance of inertial and aerodynamic forces for Tran60a44 in body axes: (a) horizontal force F_x, (b) vertical force F_z, (c) pitch moment M_y, and (d) trim solution. The horizontal and vertical forces are expressed as a percentage of the vehicle's weight. The pitch moment is expressed as a percentage of the vehicle's weight times the horizontal tail span. The sign of the percentage corresponds to the sign of the force.

To finalize the analysis of this flight condition, the blade section normal force coefficient $M^2 c_n$ is presented in figure 22. Since the influence of the vortices on the proprotors is less pronounced, there is a less strong radial variation of the normal force near the tip. In this case, the azimuthal variations are likely due to differences in the in-plane velocity, which affects the angle of attack of the sections. As a consequence, for proprotors 1, 3, and 5, the maximum $M^2 c_n$ appears on the advancing side, near $\psi \approx 90°$. It is possible that interactions with the adjacent proprotor are responsible for extending the peaks near the tip past to $\psi \approx 225°$ for proprotors 1 and 3. In the case of proprotor 7, rotor-wake interactions cause sudden changes of $M^2 c_n$ in the second and third quadrants.

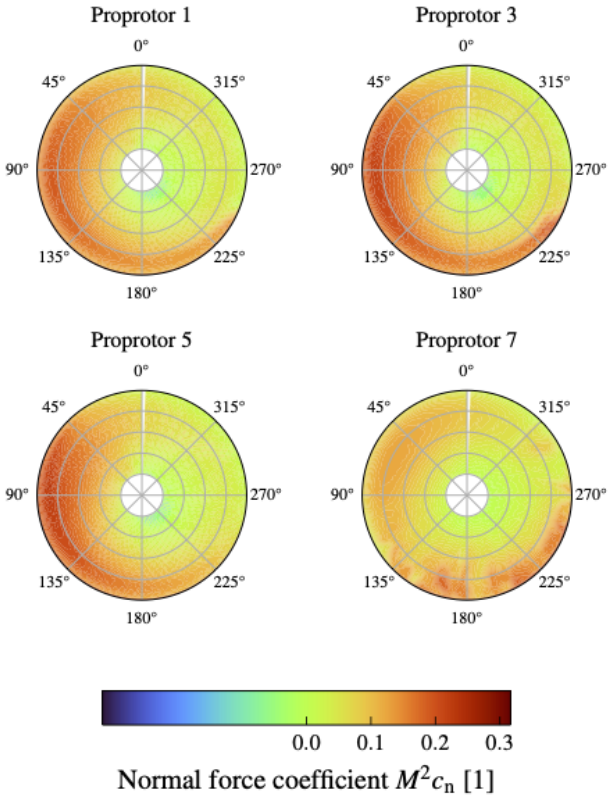

Figure 22: Sectional normal force coefficient $M^2 c_n$ distribution for Tran60a44.

Airplane mode at 110 knots, Cruise110

At this point, the conversion maneuver is finalizing and the wing is locked at a tilt angle of $i_w = 0°$. The airspeed of the vehicle $V = 110\,\text{kt}$ has reached a suitable level for horizontal flight without relying solely on the proprotors for the lift function.

The wake geometry is visualized through the representation of iso-surfaces of Q-criterion colored by nondimensional vorticity magnitude in figure 23. Tip vortices, trailed from each blade, trace out helical trajectories downstream of the proprotors as a result of the combination of the axial flow passing through the proprotor disk and the rotational motion of the blades. Due to

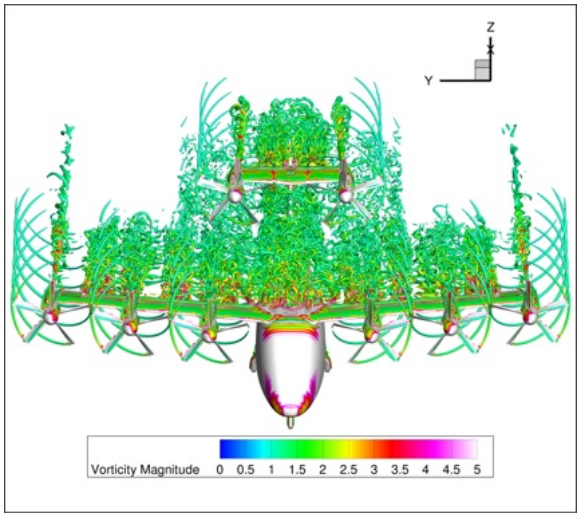

(a)

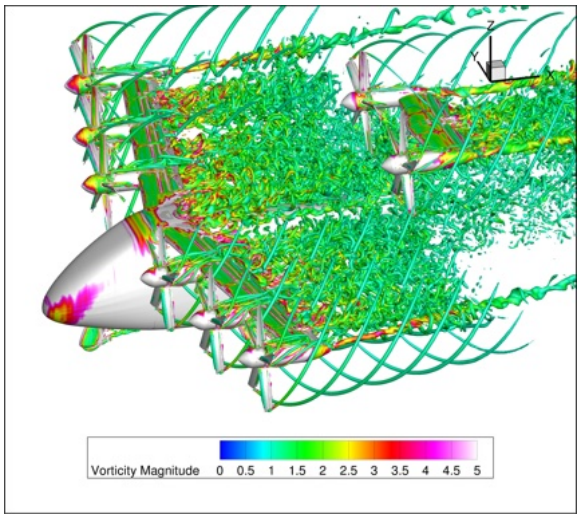

(b)

Figure 23: Snapshot in time of the iso-surfaces of Q-criterion colored with nondimensional vorticity magnitude for Cruise110: (a) front view and (b) lateral view.

the relatively high advance ratio $\mu \approx 0.62$ and low incidence $i_w = 0°$, the flow about each proprotor is predominantly axial. Rapid convection by the freestream reduces interactions with neighboring blades and between adjacent proprotors. However, the wakes of inboard proprotors are seen to impinge on tail proprotors. The spin direction of the proprotors is chosen to reduce the strength of the tip vortices from the wing and tail, trying to improve cruise performance by reducing the induced drag of the wing. A 20° deflection of the flap, which extends over 87 % of the wing span, induces flow separation across this portion of the wing. Separated flow at the fuselage-wing fairing results from the gap between them that allows the wing to rotate. The wake from the separated flow quickly disrupts the helical paths of the proprotor wakes. Since the vehicle operates at a slightly positive pitch angle, the separated wake is convected upwards and passes beneath the horizontal tail. This causes rotor-wake interactions for tail proprotors at the lower blade positions. The high deflection of the elevator also

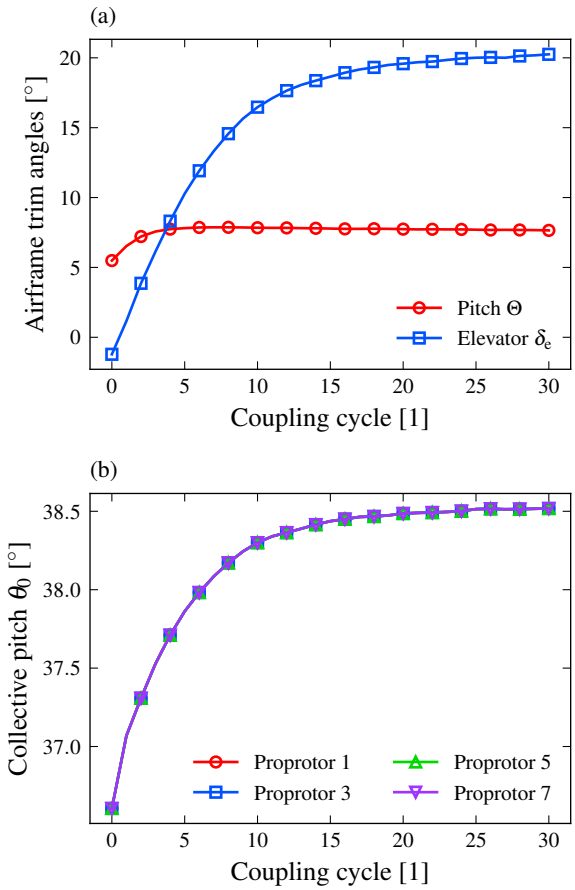

Figure 24: Convergence history of the trim angles for Cruise110: (a) airframe pitch Θ and elevator deflection δ_e, and (b) rotor collective pitch θ_0. The final trimmed values are $\Theta = 7.7°$, $\delta_e = 20.3°$, and $\theta_0 = 38.5°$.

induces significant flow separation in its wake.

In such a wing-borne regime, the control of the vehicle involves utilizing rotor collective pitch θ_0 to trim the horizontal force, pitch attitude Θ to trim the vertical force, and elevator deflection δ_e to trim the pitch moment. The time history of these variables is plotted in figure 24. The airframe pitch stabilizes rapidly, achieving a steady solution in 5 OVERFLOW-CAMRAD II coupling cycles. The elevator deflection and collective pitch angle curves begin to plateau after about 20 coupling cycles. The difference in convergence rates between these variables may be related to the aerodynamic modeling in CAMRAD II and the coupling methodology. In CAMRAD II, the aerodynamic characteristics of the wing-body are defined by setting the aerodynamic lift, drag, and pitch moment at the collocation point. These quantities are updated after each iteration based on the CFD solution for the three longitudinal airloads, following equation (6). However, the aerodynamic model of the horizontal tail only considers lift and drag forces. The pitch moment about the center of gravity is the resulting action of the secondary moment generated by these forces. The convergence of the elevator deflection might be slower because three longitudinal loads need to be updated for the horizontal tail with only two variables. This effect becomes more important considering the significant variation between the initial and final trim values. Proprotor trim is not achieved until after the elevator deflection stabilizes to compensate for the increase in aerodynamic drag, although the final value does not differ much from the initial guess. All proprotors are trimmed with equal collective pitch settings.

Figure 25 presents a comprehensive summary of the trim solution. It shows the horizontal force F_x, vertical force F_z, and pitch moment M_y acting on different parts of the vehicle, expressed in body axes. The gravity component due to the weight is also included. The trim solution is detailed below:

- Along the x-axis, the equilibrium is mainly established between the gravity component ($-13.3\,\%$) and the thrust produced by the wing proprotors ($11.1\,\%$) and tail proprotors ($3.5\,\%$). This is compatible with the fact that the airframe pitch angle is slightly positive, resulting in a weight component along the negative x-axis direction. This component is compensated by the proprotors' thrust. At first glance, the nearly negligible contribution of the wing-body ($-0.4\,\%$) might appear counterintuitive, as one would expect a significant form drag from the separated flow behind the wing. However, it is important to note that this drag points in the direction of the wind, which is not aligned with the body geometry, as $\Theta \simeq \alpha_w \approx 7.6°$. When bringing the forces in wind axes to body axes, the lift component $L\sin\alpha$ and the drag component $-D\cos\alpha$ have a canceling effect.

- Along the z-axis, the fundamental contributions are due to the gravity component ($99.1\,\%$), the wing-body ($-77.2\,\%$), and to a lesser extent, the horizontal tail ($-13.1\,\%$) and the wing proprotors ($-8.1\,\%$). In this case, the contributions of lift $-L\cos\alpha$ and drag $-D\sin\alpha$ point in the negative direction of the axis, but $L\cos\alpha \gg D\sin\alpha$. Essentially, the trim along the z-axis indicates that the weight of the vehicle is balanced by the lift produced by the wing and horizontal tail.

- Along the y-axis, the balance of pitch moment implies the equilibrium of the nose-up moments produced by the wing-body ($16.9\,\%$) and wing proprotors ($2.6\,\%$), and the nose-down moments produced by the horizontal tail ($-16.7\,\%$) and tail proprotors ($-3.3\,\%$). The center of gravity is located between the wing and the tail. Implication on the static stability of the vehicle is out of the scope of the present work.

For supplementary reference, a table with the values used to produce the bar plots is also shown. The trim solution is achieved with less than 1 % error. This error is calculated as a percentage of the sum of the absolute values of the total force along each axis. This flight condition is more favorable for convergence compared to any of the transition cases, since the flow remains mostly attached over the wing.

In order to investigate the blade loading distribution, figures 26 and 27 show contour maps of the sectional normal force coefficient $M^2 c_n$ and pitch moment coefficient $M^2 c_m$. The blade

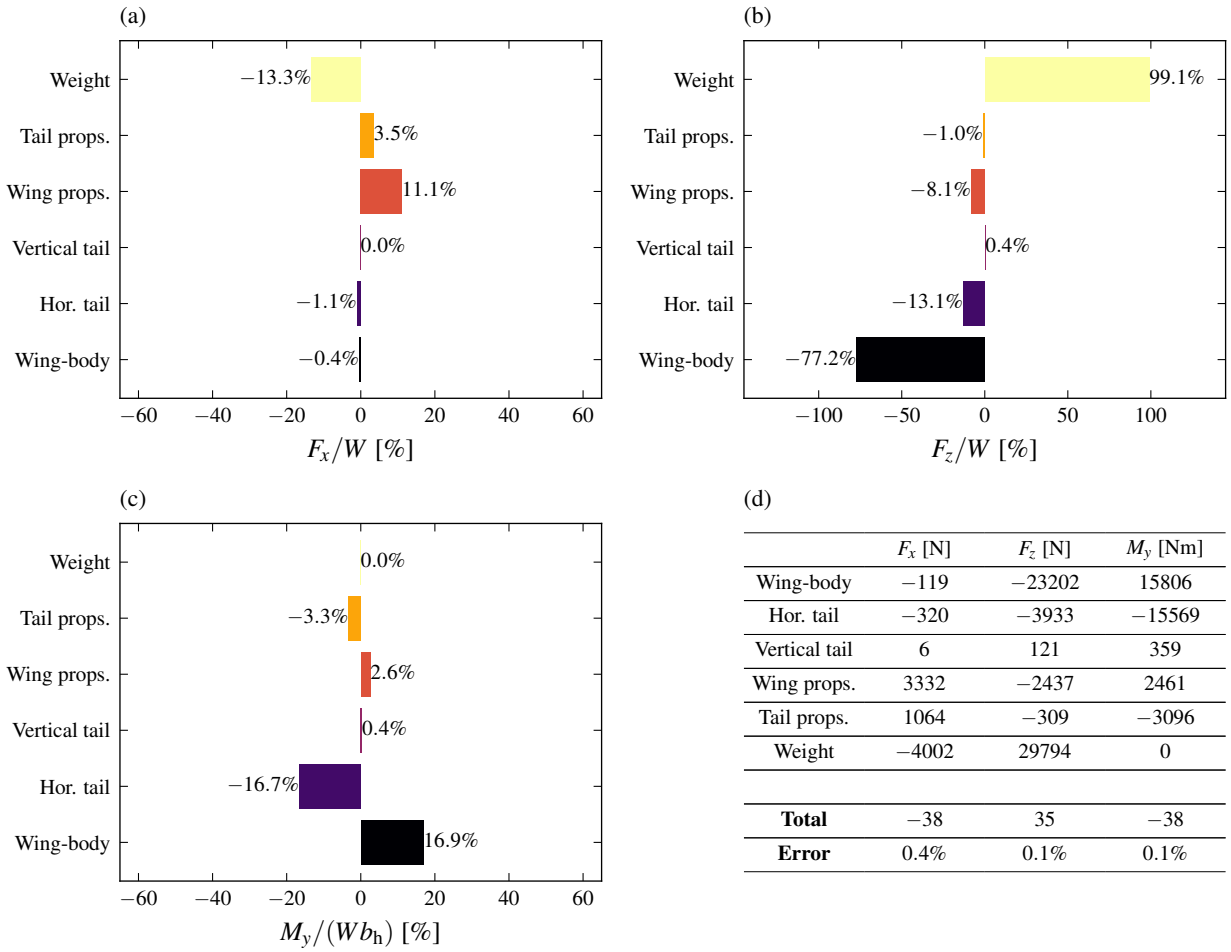

(d)

	F_x [N]	F_z [N]	M_y [Nm]
Wing-body	−119	−23202	15806
Hor. tail	−320	−3933	−15569
Vertical tail	6	121	359
Wing props.	3332	−2437	2461
Tail props.	1064	−309	−3096
Weight	−4002	29794	0
Total	−38	35	−38
Error	0.4%	0.1%	0.1%

Figure 25: Balance of inertial and aerodynamic forces for Cruise110 in body axes: (a) horizontal force F_x, (b) vertical force F_z, (c) pitch moment M_y, and (d) trim solution. The horizontal and vertical forces are expressed as a percentage of the vehicle's weight. The pitch moment is expressed as a percentage of the vehicle's weight times the horizontal tail span. The sign of the percentage corresponds to the sign of the force.

azimuth angle ψ is measured in shaft axes from the x direction, positive in the direction of proprotor rotation. In figure 26, the distribution patterns of M^2c_n for proprotors 1, 3, and 5 are characterized by a loading asymmetry between the downgoing and upgoing blade regions. While the blade is descending, the maximum M^2c_n appears in the region $r/R \approx 0.85$, for $90^\circ < \psi < 135^\circ$. While ascending, the blade experiences a negative M^2c_n in the region $0.2 < r/R < 0.7$, for $270^\circ < \psi < 360^\circ$. The loading asymmetry is believed to be caused primarily by variations in the local angle of attack. These changes can be traced back to the effects of the edgewise component of the freestream velocity and the wing induced upwash. Indeed, as sketched in figure 28, the local blade angle of attack increases for a descending blade and decreases on the opposite side. The blade element theory provides a simple framework to estimate the blade section angle of attack without accounting for three-dimensional effects and wake interactions. Considering the relative velocity to a cross-section of the blade depicted in figure 28, the aerodynamic angle of attack α is the difference between the pitch angle θ and the inflow angle ϕ:

$$\alpha = \theta - \phi = \theta - \operatorname{atan}\frac{V_x + v_i}{\Omega r + V_z \sin\psi}. \tag{7}$$

The pitch angle is the sum of the collective pitch and geometric twist —note that the cyclic pitch angles are zero. The inflow angle is determined by the components of the local velocity vector: the normal velocity consists of the normal component of the freestream velocity V_x and the induced velocity v_i; the in-plane velocity is the sum of the edgewise component of the freestream velocity V_z and the rotation of the blades at rate Ω. The relative in-plane velocity increases on the descending side of the proprotor disk, resulting from the combined effects of rotational speed and edgewise velocity. This velocity peaks at $\psi \approx 90^\circ$, reaching a maximum value of $\Omega r + V_z$. As a consequence, the increased velocity leads to higher angles of attack and enhanced lift generation. On the retreating side, the blade experiences a decreased in-plane velocity. The minimum value $\Omega r - V_z$ occurs at $\psi \approx 270^\circ$. This results in lower angles of attack and reduced lift generation. The effect of lowering the angle of attack is further aggravated in sections near the

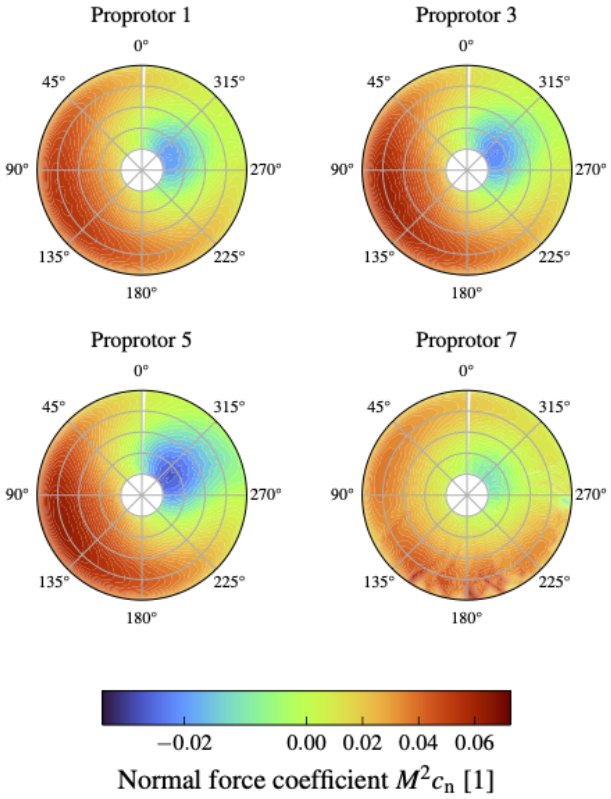

Figure 26: Sectional normal force coefficient M^2c_n distribution for Cruise110.

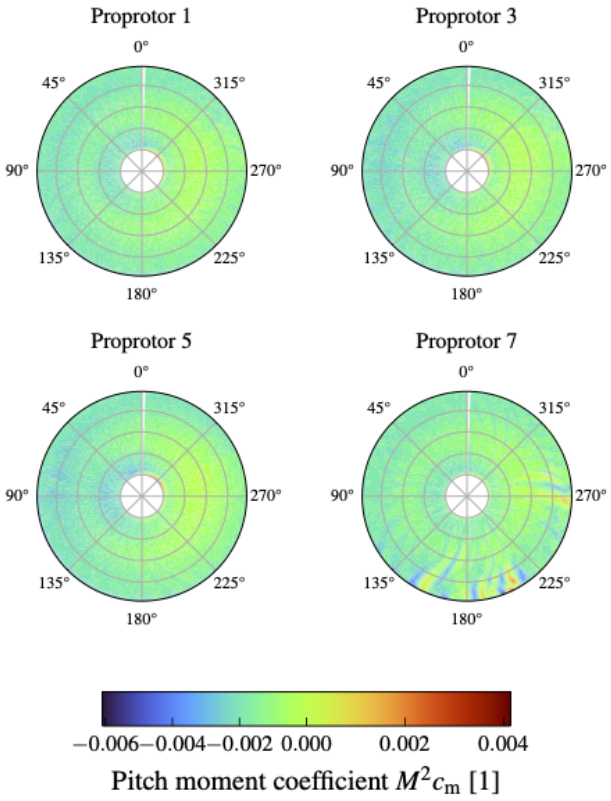

Figure 27: Sectional pitch moment coefficient M^2c_m distribution for Cruise110.

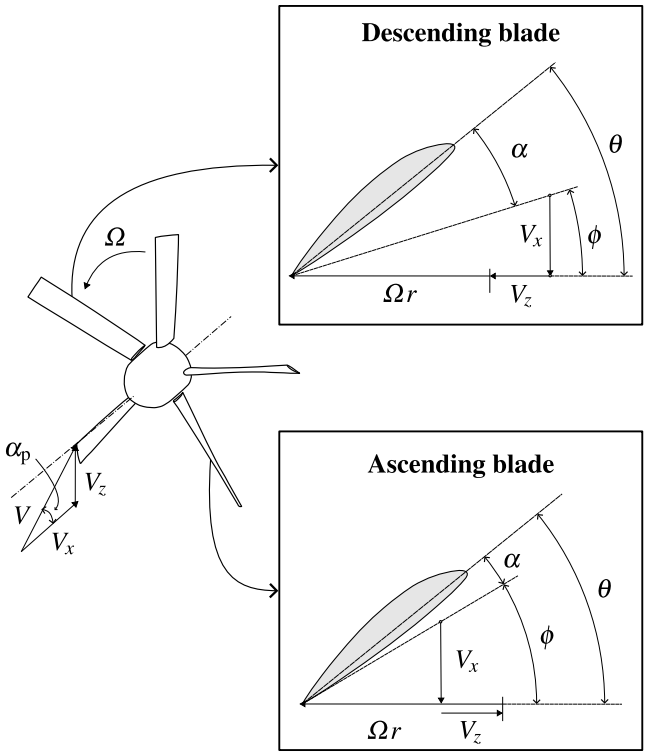

Figure 28: Variation of the local blade angle of attack α.

root, where the rotational component is smaller. The actual azimuthal locations of the maximum and minimum angles of attack will vary depending on the aerodynamic interference from other components, but this discussion contributed to explaining the values of M^2c_n. Proprotor 5 is greatly affected by the fuselage, which makes the downward force area extend to a larger midspan region. In that regard, the differences between proprotors 1 and 3 are less pronounced. Proprotor 7 is partially immersed in the wake of the separated flow coming from upstream components, which is reflected in impulsive changes of the M^2c_n for azimuths in the range $135° < \psi < 225°$.

In figure 27, the contour maps of M^2c_m are more uniformly distributed. Rotor-wake interactions induce strong fluctuations in the pitch moment for proprotor 7, spanning the range $135° < \psi < 270°$.

Figure 29 shows the time-averaged radial distribution of normal force coefficient $\overline{M^2c_n}$ and pitch moment coefficient $\overline{M^2c_m}$ over the period of one rotor revolution. The mean normal force increases along the blade span, peaking around $r/R = 0.85$, before gradually decreasing. The sharp increase near the tip is caused by the development of the tip vortex on the upper surface of the blade, a phenomenon also observed in transitional flight —see figure 16. A net downward normal force is observed near the blade root. The blades experience a pitch down moment throughout their span with a strong negative moment towards the blade tip due to the vortex core influence. There are no significant differences between wing and tail proprotors.

To finalize the blade loading analysis, figure 29 shows the azimuthal distributions of M^2c_n and M^2c_m —mean removed— for two radial stations at $r/R = 0.5$ and $r/R = 0.9$. The am-

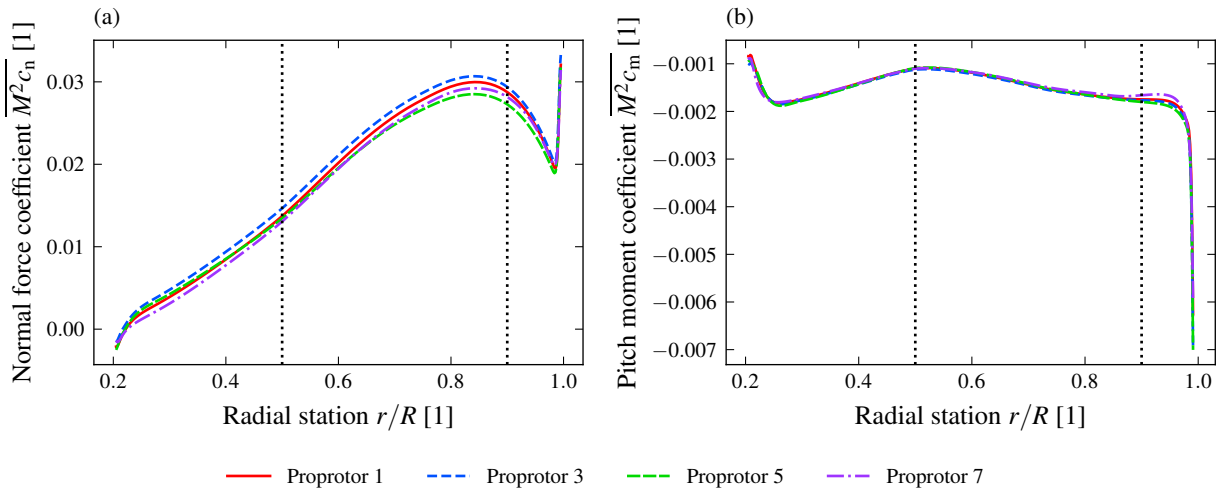

Figure 29: Radial distribution of airloads for Cruise110: (a) normal force coefficient $M^2 c_n$ and (b) pitch moment coefficient $M^2 c_m$. The radial stations $r/R = 0.5$ and $r/R = 0.9$ are marked with dashed lines to indicate the mean value used to normalize the azimuthal distributions.

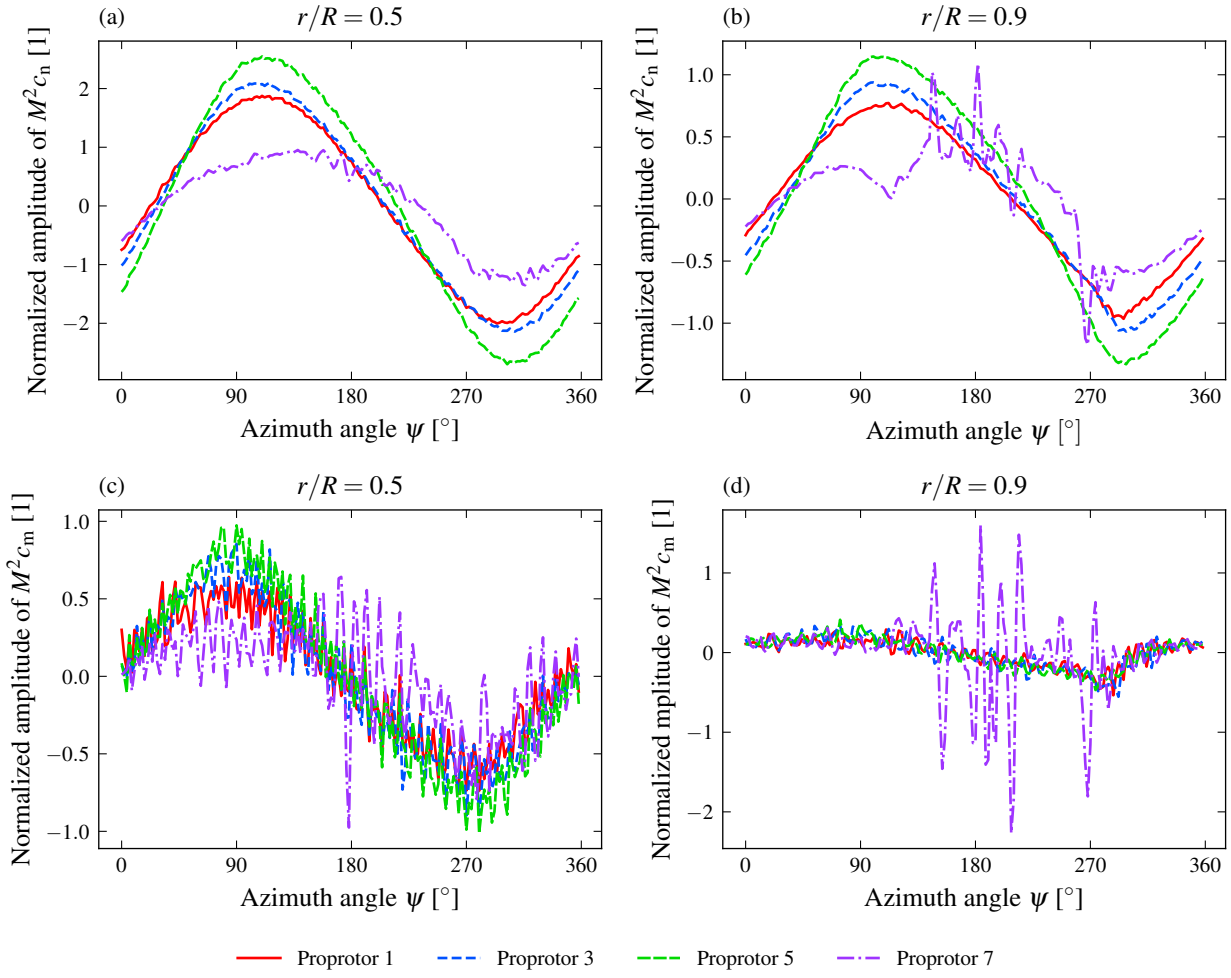

Figure 30: Azimuthal distribution of the fluctuations of the airloads for Cruise110: (a) normal force coefficient $M^2 c_n$ at $r/R = 0.5$, (b) normal force coefficient $M^2 c_n$ at $r/R = 0.9$, (c) pitch moment coefficient $M^2 c_m$ at $r/R = 0.5$, and (d) pitch moment coefficient $M^2 c_m$ at $r/R = 0.9$. The mean is removed and the fluctuations are normalized by the mean value at the corresponding radial station.

plitude of the oscillations is normalized by the mean. Some features observed are:

- At the midspan station $r/R = 0.5$, the normal force shows a periodic behavior with respect to the azimuth. In the case of wing proprotors, the oscillation amplitudes grow larger closer to the fuselage, reaching a peak over 200 % of the mean value for proprotor 5, and slightly lower values for proprotors 1 and 3. The maximum of the $M^2 c_n$, occurring shortly after $\psi = 90°$, is approximately three times the mean force. Conversely, the minimum of $M^2 c_n$, which occurs shortly after $\psi = 270°$, is comparable to the mean force in absolute value. The half-peak amplitude for proprotor 7 is approximately 100 % of the mean. Aerodynamic interactions with the wake of the wing and wing proprotors likely account for the different amplitude observed for tail proprotors. The pitch moment also exhibits a quasi-periodic behavior, with noticeable unsteady fluctuations, particularly for proprotor 7. The amplitude of the oscillations is similar for all proprotors, reaching as much as 100 % of the mean.

- At the outboard station $r/R = 0.9$, there is a tendency for the oscillation amplitude to decrease. This is due to less pronounced variations of the angle of attack, since the rotational velocity is higher. Rotor-wake interactions, as observed in figure 23, induce impulsive changes in the normal force and pitch moment for proprotor 7 in the azimuthal range $135° < \psi < 270°$. In this scenario, the oscillations are stronger compared to those at the midspan section. For the normal force, they are similar in magnitude to those of the wing proprotors, hovering around 100 % of the mean. For the pitch moment, they exceed 200 % of the mean. These results suggest that rotor-wake interactions have a more impactful effect on the pitch moment than on the normal force. The rapid change between pitch up and pitch down moments may cause significant vibratory loads.

Airplane mode at 155 knots, Cruise155

This condition aims to be representative of the cruise segment of the mission profile, where the tiltwing vehicle is in a state of level flight at the designated altitude. The best-range speed $V = 155\,\text{kt}$ was determined by NDARC modeling. During the acceleration from the previous flight condition, the wing remains locked at $i_w = 0°$, the flap moves to an undeflected position, while the airframe pitch, rotor collective, and elevator deflection are adjusted to maintain stability.

Figure 31 shows the iso-surfaces of Q-criterion colored by nondimensional vorticity magnitude. The wake structure is similar to that of Cruise110 —see figure 23. The flow through the proprotor disks is predominantly axial, with a small tangential component due to the aircraft pitch angle $\Theta \approx 6°$. The proprotor wakes describe a helical path that is disrupted by interactions with the wing and tail. The tip vortices are more widely spaced in the axial direction due to a higher advance ratio $\mu \approx 0.87$, leading to a less strong influence on the rotors. In this condition, the wing flap is undeflected, which reduces the separated flow behind the wing. The vortical structures observed are trailed from the flap slot. The tail proprotors operate in a less turbulent environment, experiencing reduced wake interference. Two pairs of counter-rotating "tip" vortices are trailed from the elevator split sections of the tailspan.

Several design decisions for this vehicle were made to optimize cruise performance. For example, the shaft axes of the outboard wing proprotors are aligned with the wing chord to assist in counteracting the wingtip vortices —recall that the spin direction of the proprotors opposes that of the tip vortices. This has potential to reduce the induced drag. The middle and inboard wing proprotors are positioned slightly below the chord, aiming to reduce the influence of the nacelle on the leading edge suction peak of the wing (Ref. 4). Dedicated analyses of proprotor-wing interactions are required to quantify these effects. With a focus on cruise conditions, a wind tunnel

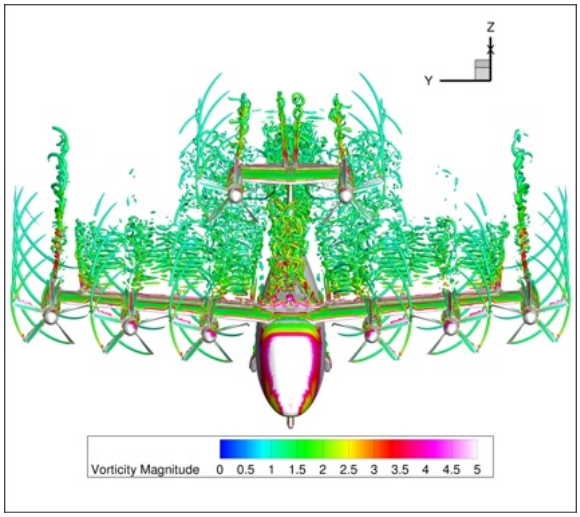

(a)

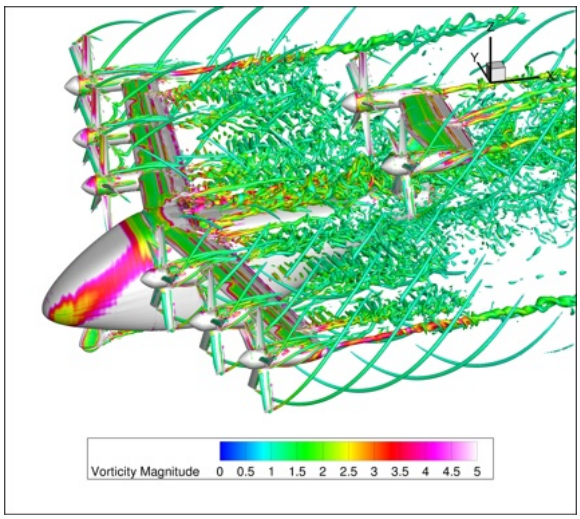

(b)

Figure 31: Snapshot in time of the iso-surfaces of Q-criterion colored with nondimensional vorticity magnitude for Cruise155: (a) front view and (b) lateral view.

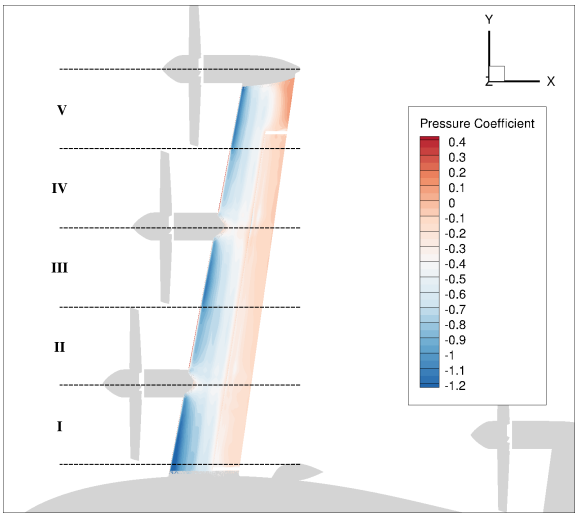

Figure 32: Snapshot in time of the pressure coefficient distribution on the upper surface of the wing for Cruise155.

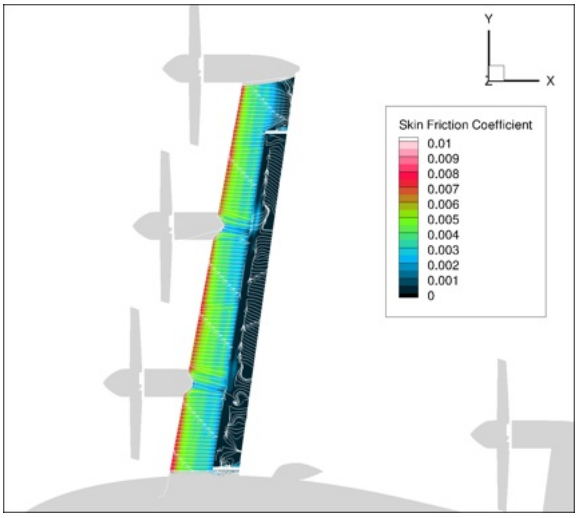

Figure 33: Snapshot in time of the streamtraces and the skin friction coefficient distribution on the upper surface of the wing for Cruise155.

test campaign is projected at the NASA Langley 14×22-foot subsonic wind tunnel, as well as CFD simulations to support the experimental efforts. Some of the results from the present study may offer an initial understanding of the interactional aerodynamics, aiding in prioritizing relevant test conditions.

For instance, figure 32 shows the pressure coefficient distribution on the upper surface of the wing. Considering the influence of the slipstream, the wing can be divided into five regions roughly delimited by the edges of the proprotors and the centerlines of the nacelles. Regions I, III, and V are washed by the wake of the ascending blades; whereas regions II and IV are affected by the descending blades. The pressure coefficient contour clearly shows how the suction peak is enhanced in the former. The slipstream effect on the wing is twofold. Firstly, the axial component of the proprotor wake increases the dynamic pressure of the flow over the wing, both in the upper and lower surfaces, which enhances lift generation. This

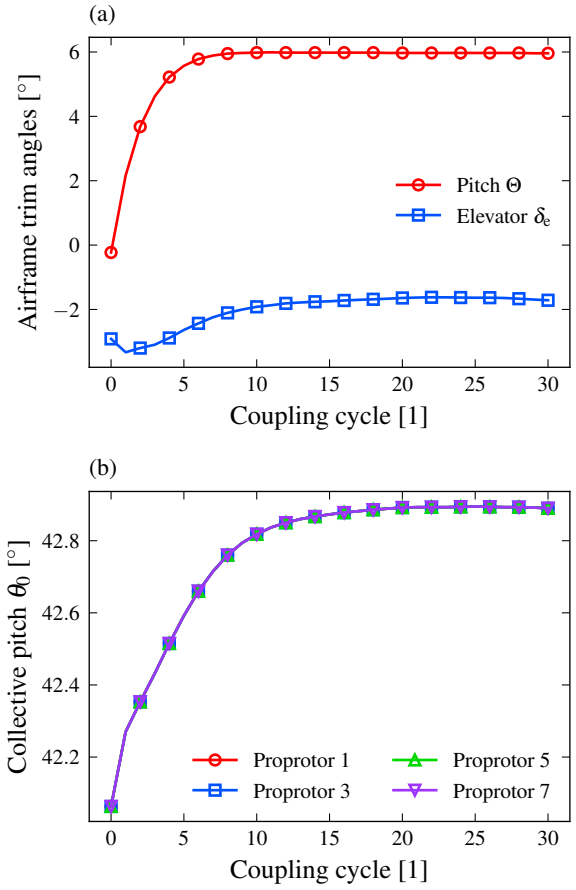

Figure 34: Convergence history of the trim angles for Cruise155: (a) airframe pitch Θ and elevator deflection δ_e, and (b) rotor collective pitch θ_0. The final trimmed values are $\Theta = 6°$, $\delta_e = -1.7°$, and $\theta_0 = 42.9°$.

phenomenon occurs within the contracted vein; however, because the wing proprotors are laterally tangential, the wing is blown uniformly across the span. Secondly, the rotational motion of the blades induces opposing variations of the angle of attack of the wing. In regions I, III, and V, the upwash of the ascending blade locally increases the angle of attack, which further augments lift. In regions II and IV, the downwash of the descending blade decreases the local angle of attack, which partially reduces the effect of the raise in dynamic pressure. To optimize lift generation, it is generally preferable to displace the increase of dynamic pressure towards the upper surface. Research by Veldhuis (Ref. 32) on propeller-wing interactions concluded that higher positioned propeller configurations achieve greater lift, although in their work the nacelle was detached from the wing. They also note that lower propeller configurations proved beneficial in terms of propulsive efficiency, as well as horizontally spacing the proprotors. The positioning of the proprotors can significantly affect vehicle performance. A study of different horizontal and vertical placements of the proprotors on the wing is left for future work.

Performance and controllability may be compromised by flow separation over the wing. Figure 33 shows the surface streamlines and the skin friction coefficient distribution on the upper

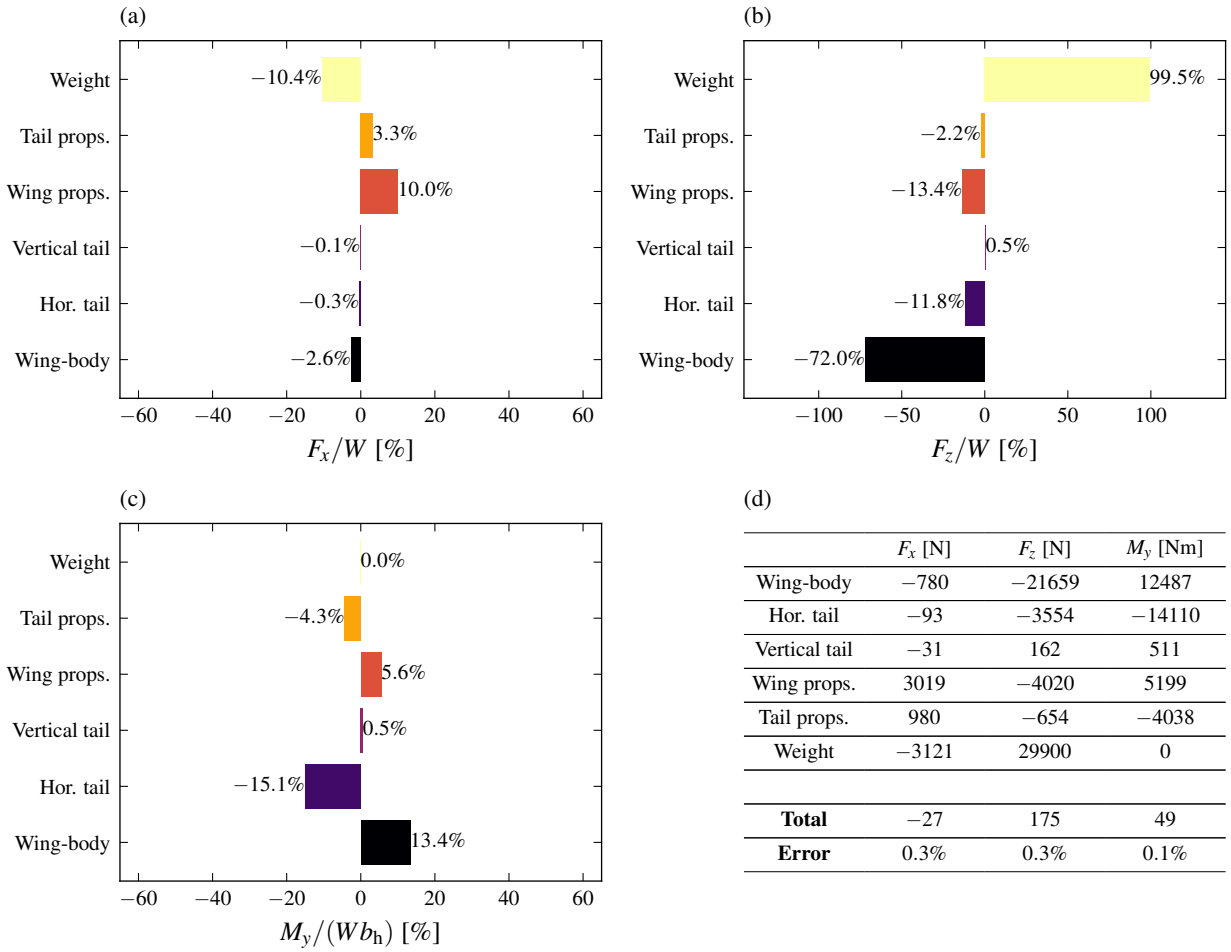

(d)

	F_x [N]	F_z [N]	M_y [Nm]
Wing-body	−780	−21659	12487
Hor. tail	−93	−3554	−14110
Vertical tail	−31	162	511
Wing props.	3019	−4020	5199
Tail props.	980	−654	−4038
Weight	−3121	29900	0
Total	−27	175	49
Error	0.3%	0.3%	0.1%

Figure 35: Balance of inertial and aerodynamic forces for Cruise155 in body axes: (a) horizontal force F_x, (b) vertical force F_z, (c) pitch moment M_y, and (d) trim solution. The horizontal and vertical forces are expressed as a percentage of the vehicle's weight. The pitch moment is expressed as a percentage of the vehicle's weight times the horizontal tail span. The sign of the percentage corresponds to the sign of the force.

surface of the wing, aiming to identify areas of flow separation and other flow features of interest. Most of the flow remains attached to the main wing, although a small region of separation is observed near the tip. This separation is induced by the vortical structures generated at the flap cut. Behind the outboard nacelle, the flow remains attached but sweeps longitudinally inward. Vortices coming from the middle and inboard nacelles contribute to a reduction in local skin friction coefficient for wing sections located behind them. Flow separation is observed over the upper surface of the flap, which potentially reduces the effectiveness of the control surface. As previously mentioned, a slotted flap design was chosen to facilitate mesh generation. However, a design that offers a smoother transition between the wing and flap chords will likely mitigate flow separation at small to moderate angles of attack. A comparison with oil flow patterns from experiments is required to ascertain the agreement or disagreement of these separated flow regions.

In order to examine the trim solution, figure 34 shows the time history of the airframe pitch attitude Θ, elevator deflection δ_e, and rotor collective pitch θ_0. The trim variables are mostly "settled" after 10 OVERFLOW-CAMRAD II coupling cycles. The convergence is thought to be faster than in Cruise110 because of the reduced flow separation from the wing. However, it seems that the tendency of a slower convergence for the elevator persists, as seen by a more gradual slope of the curve. Notice the large reduction of the elevator deflection compared to Cruise110. In this scenario, the pitch angle is also lower. As the vehicle gains speed, it adopts a more horizontal position, facilitated by the ability of the wing to produce sufficient lift at a lower angle of attack. Despite that fact, both values are very similar, since in the previous condition, lift was augmented by deploying the flap. Finally, the collective pitch slightly increases. This adjustment is necessary to maintain a positive blade section angle of attack, as the increased axial flow tends to reduce it —see equation (7).

Figure 35 presents the contribution of each component to the generation of inertial and aerodynamic actions on the vehicle. The values are expressed in body axes. The trim solution, achieved with less than 1 % error, is detailed below:

- Along the x-axis, the gravity component (−10.4 %) and

the aerodynamic action on the wing-body (−2.6 %) are primarily compensated by the propulsive force generated by the wing proprotors (10.0 %) and tail proprotors (3.3 %). Compared to Cruise110, the percentage split of the proprotors largely remains unchanged, since these are the only components generating force in the positive axis direction. In the case of the weight and wing-body contributions, the change is primarily driven by the pitch attitude. For the latter, the lift and drag remain comparable, but when the vehicle adopts a more horizontal position, the lift projection in the positive direction of the axis decreases.

- Along the z-axis, the fundamental contributions are due to the gravity component (99.5 %), the wing-body (−72.0 %), and to a lesser extent, the horizontal tail (−11.8 %) and the wing proprotors (−13.4 %). These percentages are largely similar to those observed in Cruise110.

- Along the y-axis, the wing-body (13.4 %) and wing proprotors (5.6 %) generate nose-up pitch moments, which are balanced by the nose-down moments produced by the horizontal tail (−15.1 %) and tail proprotors (−4.3 %). When compared to Cruise110, there is a decrease in the contributions of the wing-body and horizontal tail in favor of wing and tail proprotors. The decrease in the former can be explained by a smaller amount of deflection of the control surfaces. The increase in the latter is due to larger drag forces that result in larger secondary moments about the center of gravity.

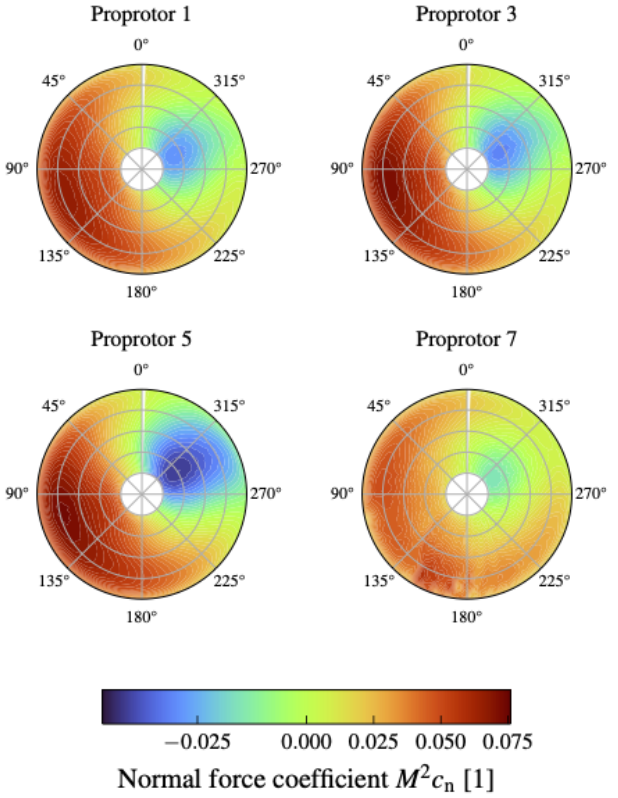

Figure 36: Sectional normal force coefficient M^2c_n distribution for Cruise155.

To conclude the analysis of this flight condition, figure 36 shows the contour map of the blade section normal force coefficient M^2c_n. The sectional loading exhibits the same features described for Cruise110. There is a marked lateral asymmetry due to the differences in the angle of attack for ascending and descending blades. For proprotors 1, 3, and 5, the maximum and minimum (negative) forces appear in similar radial and azimuthal locations. The effect of increasing the forward velocity extends the negative M^2c_n region to outer radial stations, especially for proprotor 5. In the case of proprotor 7, the influence of interactions with the separated wake diminishes both in magnitude and extent.

CONCLUDING REMARKS

This paper explored the use of high-fidelity CFD to simulate NASA's tiltwing air taxi concept in transition flight. Different points along a predefined transition corridor were analyzed by loosely coupling the CFD flow solver OVERFLOW and the rotorcraft comprehensive code CAMRAD II. The trim solutions of two control states were examined: (1) for a rotor-borne regime, the vehicle is trimmed with mean and differential rotor collective pitch and pitch attitude; (2) for a wing-borne regime, the vehicle is trimmed with equal rotor collective pitch, elevator deflection, and pitch attitude. Flow visualizations were extracted from the CFD solutions to discuss the impact of interactional aerodynamics on vehicle performance.

To conduct the simulations, a novel coupling capability was built upon the traditional rotor-focused coupling methodology. This new capability allows the CFD aerodynamics of the entire vehicle to update the comprehensive code aerodynamics, aiming to improve the trim solution. This approach was demonstrated for different stages of the transition maneuver. From the results presented, the following conclusions can be made:

- To quantify the trim solution accuracy, the errors were measured as a percentage of the sum of the absolute values of the horizontal force, vertical force, and pitch moment in body axes. In airplane mode, the trim solution is achieved with excellent accuracy, with errors consistently falling below 1 %. In transition mode, while this tendency remains for the horizontal and vertical forces, the errors in pitch moment reach up to 10 %. This could be attributed to unsteady aerodynamic loading on the tail, induced by separated flow over the wing at high incidence angles. To mitigate this effect, it is recommended to increase the averaging period on the pitch axis.

- The blade loading of the wing proprotors is characterized by a marked lateral asymmetry. During the early stages of transition, this asymmetry is primarily caused by the influence of nearby vortices, which induce a marked radial variation of the loads near the tip. As the proprotors align with the freestream, these interactions become weaker as

the axial separation of the vortices increases. In this case, the asymmetry extends through a larger spanwise region of the blades, and is primarily caused by changes in the angle of attack between the advancing and the retreating sides. While these effects occur on a smaller scale in the tail proprotors, their interactions with the wake lead to strong, impulsive fluctuations of the loads.

- Rotor-wing aerodynamic interactions can be harnessed to control flow separation over the wing. The blowing effect of the slipstream is generally beneficial as it energizes the flow. In contrast, the swirling motion has opposing effects: wing sections located behind descending blades benefit from a downwash that improves flow attachment, whereas wing sections located behind ascending blades encounter an upwash that promotes premature flow separation. To address the latter effect, utilizing flow control devices, such as leading-edge slats, could prove effective.

- High-fidelity CFD methods capture complex aerodynamic interactions and provide a broad range of flowfield details that can be investigated to improve vehicle design and performance.

Overall, the results obtained provide valuable insights into the complex aerodynamic interactions that occur in transition flight, and can help in prioritizing relevant test conditions. Future work will focus on supporting experimental efforts.

ACKNOWLEDGMENTS

This work is supported by the Revolutionary Vertical Lift Technology (RVLT) project (PM: Noah Schiller; TL: Brian Allan). The computations utilized the Pleiades, Electra, and Aitken supercomputers at the NASA Advanced Supercomputing Division. The authors would like to thank Wayne Johnson, Chris Silva, Jason Welstead, and Brian Allan for helpful discussions.

REFERENCES

1. Yamauchi, G., "A Summary of NASA Rotary Wing Research: Circa 2008–2018," Technical Report NASA/TP-2019-220459, NASA, December 2019.

2. Johnson, W., and Silva, C., "Observations from Exploration of VTOL Urban Air Mobility Designs," 7th Asian/Australian Rotorcraft Forum, October 30 – November 1 2018.

3. Silva, C. J., and Johnson, W., "Practical Conceptual Design of Quieter Urban VTOL Aircraft," 77th VFS Annual Forum and Technology Display, 2021.

4. Whiteside, S., Pollard, B., Antcliff, K., Zawodny, N., Fei, X., Silva, C., and Medina, G., "Design of a Tiltwing Concept Vehicle for Urban Air Mobility," Technical Report NASA/TM–20210017971, NASA, June 2021.

5. Johnson, W., Silva, C. J., and Solis, E., "Concept Vehicles for VTOL Air Taxi Operations," Paper ARC-E-DAA-TN50731, AHS Specialists Conference on Aeromechanics Design for Transformative Vertical Flight, 2018.

6. Pradeep, P., and Wei, P., "Energy Optimal Speed Profile for Arrival of Tandem Tilt-Wing eVTOL Aircraft with RTA Constraint," 2018 IEEE CSAA Guidance, Navigation and Control Conference (CGNCC), 2018. DOI: 10.1109/GNCC42960.2018.9018748.

7. Chauhan, S. S., and Martins, J. R. R. A., "Tilt-Wing eVTOL Takeoff Trajectory Optimization," *Journal of Aircraft*, Vol. 57, (1), 2020, pp. 93–112. DOI: 10.2514/1.C035476.

8. Panish, L., and Bacic, M., "Transition Trajectory Optimization for a Tiltwing VTOL Aircraft with Leading-Edge Fluid Injection Active Flow Control," AIAA SCITECH 2022 Forum, January 2022. DOI: 10.2514/6.2022-1082.

9. Droandi, G., Syal, M., and Bower, G., "Tiltwing Multi-Rotor Aerodynamic Modeling in Hover, Transition and Cruise Flight Conditions," AHS International 74th Annual Forum and Technology Display, May 2018.

10. Ventura Diaz, P., Garcia Perez, D., and Yoon, S., "Computational Analysis of a Quiet Single-Main Rotor Helicopter for Air Taxi Operations," 78th VFS Annual Forum and Technology Display, May 2022.

11. Ventura Diaz, P., Garcia Perez, D., and Yoon, S., "Multi-Fidelity Computational Analysis of a Quiet Single-Main Rotor Helicopter for Air Taxi Operations," AIAA AVIATION 2023 Forum, 2023. DOI: 10.2514/6.2023-3669.

12. Ventura Diaz, P., and Yoon, S., "Computational Study of NASA's Quadrotor Urban Air Taxi Concept," AIAA SCITECH 2020 Forum, 2020. DOI: 10.2514/6.2020-0302.

13. Ventura Diaz, P., and Yoon, S., "High-Fidelity Simulations of a Quadrotor Vehicle for Urban Air Mobility," AIAA SCITECH 2022 Forum, 2022. DOI: 10.2514/6.2022-0152.

14. Ventura Diaz, P., Johnson, W., Ahmad, J., and Yoon, S., "Computational Study of the Side-by-Side Urban Air Taxi Concept," 75th VFS Annual Forum and Technology Display, May 2019.

15. Ventura Diaz, P., Johnson, W., Ahmad, J., and Yoon, S., "The Side-by-Side Urban Air Taxi Concept," AIAA Aviation 2019 Forum, 2019. DOI: 10.2514/6.2019-2828.

16. Garcia Perez, D., Ventura Diaz, P., and Yoon, S., "High-Fidelity Simulations of a Tiltwing Vehicle for Urban Air Mobility," AIAA SCITECH 2023 Forum, 2023. DOI: 10.2514/6.2023-2282.

17. Garcia Perez, D., Ventura Diaz, P., Ahmad, J., and Yoon, S., "A Comparison of Rotor Disk Modeling and Blade-Resolved CFD Simulations for NASA's Tiltwing Air Taxi," 79th VFS Annual Forum and Technology Display, 2023.

18. Pulliam, T., "High Order Accurate Finite-Difference Methods: as seen in OVERFLOW," 20th AIAA Computational Fluid Dynamics Conference, 2011. DOI: 10.2514/6.2011-3851.

19. Chan, W., III, R. G., Rogers, S., and Buning, P., "Best Practices in Overset Grid Generation," Paper AIAA 2002-3191, 32nd AIAA Fluid Dynamics Conference, 6th Symposium on Overset Grids and Solution Technology, 2002. DOI: 10.2514/6.2002-3191.

20. Johnson, W., "Rotorcraft Aerodynamics Models for a Comprehensive Analysis," American Helicopter Society 54th Annual Forum, May 1998.

21. Haimes, R., and Dannenhoffer, J., "The Engineering Sketch Pad: A Solid-Modeling, Feature-Based, Web-Enabled System for Building Parametric Geometry," 21st AIAA Computational Fluid Dynamics Conference, 2013. DOI: 10.2514/6.2013-3073.

22. Maisel, M. D., *The History of the XV-15 Tilt Rotor Research Aircraft: From Concept to Flight*, Paper 17, National Aeronautics and Space Administration, Office of Policy and Plans, NASA History Division, 2000.

23. Pulliam, T. H., and Chaussee, D. S., "A diagonal form of an implicit approximate-factorization algorithm," *Journal of Computational Physics*, Vol. 39, (2), 1981, pp. 347–363. DOI: https://doi.org/10.1016/0021-9991(81)90156-X.

24. Spalart, P., and Allmaras, S., "A one-equation turbulence model for aerodynamic flows," 30th Aerospace Sciences Meeting and Exhibit, 1992. DOI: 10.2514/6.1992-439.

25. Spalart, P., "Comments on the Feasibility of LES for Wings, and on a Hybrid RANS/LES Approach," The AFOSR International Conference on DNS/LES, 1997.

26. Spalart, P., "Strategies for turbulence modelling and simulations," *International Journal of Heat and Fluid Flow*, Vol. 21, (3), 2000, pp. 252–263. DOI: https://doi.org/10.1016/S0142-727X(00)00007-2.

27. Potsdam, M., Yeo, H., and Johnson, W., "Rotor Airloads Prediction Using Loose Aerodynamic/Structural Coupling," *Journal of Aircraft*, Vol. 43, (3), 2006, pp. 732–742. DOI: 10.2514/1.14006.

28. Gladfelter, M., He, C., Saberi, H., Malpica, C., Johnson, W., and Silva, C., "Enhanced Flight Dynamics Models with Aerodynamic Interference for Real-Time Simulation of VTOL Concept Vehicles," 79th VFS Annual Forum and Technology Display, 2023.

29. Du Val, R., and He, C., "FLIGHTLAB modeling for real-time simulation applications," *International Journal of Modeling, Simulation, and Scientific Computing*, Vol. 08, (04), 2017, pp. 1743003. DOI: 10.1142/S1793962317430036.

30. Johnson, W., "NDARC NASA Design and Analysis of Rotorcraft," Technical Report NASA/TP—2015–218751, NASA, April 2015.

31. Marsh, K. R., "Propeller V/STOL Aircraft," *Annals of New York Academy of Sciences*, Vol. 154, 1968, pp. 856–871.

32. Veldhuis, L. M., "Review of Propeller-Wing Aerodynamic Interference," 24th International Congress of the Aeronautical Sciences, 2004.